Supplement of Hydrol. Earth Syst. Sci., 25, 4259–4274, 2021
https://doi.org/10.5194/hess-25-4259-2021-supplement

Hydrology and Earth System Sciences
Open Access

Supplement of

Plant hydraulic transport controls transpiration sensitivity to soil water stress

Brandon P. Sloan et al.

Correspondence to: Brandon Sloan (sloan091@umn.edu) and Xue Feng (feng@umn.edu)

S1 Minimalist Analytical Solution

The analytical solution for the minimalist PHM is derived by equating supply (T_s; Eq. 1 of the article) and demand (T_d; Eq. 2-3 of the article) and solving for ψ_l^* as shown in Eq. S1 (Eq. 4 of the article).

$$
\begin{aligned}
g_{sp} \cdot (\psi_s - \psi_l) &= \frac{\psi_{l,c} - \psi_l}{\psi_{l,c} - \psi_{l,o}} \cdot T_{ww} \\
\psi_l^* &= \frac{\psi_{l,c} - \psi_{l,o}}{T_{ww} - g_{sp} \cdot \left(\psi_{l,c} - \psi_{l,o}\right)} \cdot \left(\frac{T_{ww} \cdot \psi_{l,c}}{\psi_{l,c} - \psi_{l,o}} - g_{sp} \cdot \psi_s \right) \\
\psi_l^* &= \frac{T_{ww} \cdot \psi_{l,c} - g_{sp} \cdot \psi_s \cdot \left(\psi_{l,c} - \psi_{l,o}\right)}{T_{ww} - g_{sp} \cdot \left(\psi_{l,c} - \psi_{l,o}\right)} \\
\psi_l^* &= \frac{\frac{T_{ww} \cdot \psi_{l,c}}{g_{sp}} + \psi_s \cdot \left(\psi_{l,o} - \psi_{l,c}\right)}{\frac{T_{ww}}{g_{sp}} + \left(\psi_{l,o} - \psi_{l,c}\right)}
\end{aligned}
\tag{S1}
$$

Substituting ψ_l^* back into Equation 1 of the article yields the analytical solution for the minimalist PHM (Eq. S2 and Eq. 5 in the article). Algebraic manipulations shows that the solution is simply T_d with an additional dependence on the ratio of atmospheric moisture demand and soil-plant conductance in the denominator.

$$
\begin{aligned}
T^{phm} &= g_{sp} \cdot (\psi_s - \psi_l^*) \\
&= g_{sp} \cdot \left(\psi_s - \frac{\frac{T_{ww} \cdot \psi_{l,c}}{g_{sp}} + \psi_s \cdot \left(\psi_{l,o} - \psi_{l,c}\right)}{\frac{T_{ww}}{g_{sp}} + \left(\psi_{l,o} - \psi_{l,c}\right)} \right) \\
&= g_{sp} \cdot \left(\frac{\psi_s \cdot \frac{T_{ww}}{g_{sp}} + \psi_s \cdot \left(\psi_{l,o} - \psi_{l,c}\right)}{\frac{T_{ww}}{g_{sp}} + \left(\psi_{l,o} - \psi_{l,c}\right)} - \frac{\frac{T_{ww} \cdot \psi_{l,c}}{g_{sp}} + \psi_s \cdot \left(\psi_{l,o} - \psi_{l,c}\right)}{\frac{T_{ww}}{g_{sp}} + \left(\psi_{l,o} - \psi_{l,c}\right)} \right) \\
&= T_{ww} \cdot \frac{\left(\psi_{l,c} - \psi_s\right)}{\left(\psi_{l,c} - \psi_{l,o}\right) - \frac{T_{ww}}{g_{sp}}}
\end{aligned}
\tag{S2}
$$

A key conclusion of this work relates to the nonlinearity in the PHM with respect to T_{ww}, even in the simplest case of the minimalist model. This nonlinearity can be shown formally by violating the superposition principle $T^{phm}\left(\psi_s, c_1 \cdot T_{ww,1} + c_2 \cdot T_{ww,2}\right) \neq c_1 \cdot T^{phm}\left(\psi_s, T_{ww,1}\right) + c_2 \cdot T^{phm}\left(\psi_s, T_{ww,2}\right)$. This is the fundamental difference between β and PHMs and results in the T_{ww}/g_{sp} term in the denominator of Eq. S2.

S2 LSM Description

This section lays out the land surface model (LSM) coded in MATLAB (available at https://github.com/sloan091/HESS_LSM) used for the analysis of the US-Me2 ponderosa pine AmeriFlux site. The model is a two-big-leaf, dual-source model[1] following closely the formulation laid out in the Community Land Model version 5[2] with key modifications. The general model structure for scalar transport is shown in Fig. S1 with the main modules highlighted. Here, module refers to a smaller model within the overall LSM, e.g., the Plant Hydraulics Model (PHM). The purpose of this LSM is to compare the scalar transport (temperature, water vapor, and carbon transport) scheme using PHM and empirical (β) transpiration downregulation schemes; therefore, the model is simplified to be forced at the boundaries by incoming radiation, air scalar concentrations as well as soil water availability and heat flux. We are exploring the LSM component only during the growing season, so nutrient cycling, plant demographics, snow dynamics, and phenology components—common in terrestrial biosphere models like CLM— are ignored. This section is organized by the energy balance, radiative transfer, scalar transport, transpiration downregulation, and solution schemes.

We adopt a slight modification in terminology within this LSM description section. In the main text and other sections of this supplement, the transpiration flux is represented by the variable T; however, temperature is very prevalent in the LSM equations and is traditionally represented by T. To avoid confusion and maintain consistency with the conservation of energy in the LSM, we elect to represent transpiration in energy flux units (Wm^{-2}) and label it as the latent heat flux from the canopy (LE_l), where the subscript represents the two-big-leaf approximation. Similarly the bare soil evaporation is represented (LE_g), where the subscript represents the ground. Thus, the latent heat flux (LE) is the sum of canopy and ground latent heat fluxes, which is simply evapotranspiration (ET) in energy units. The notation frees up the variable T to represent temperature.

S2.1 LSM Energy Balance

The energy balance of the soil-plant-atmosphere for the two-big-leaf, dual-source LSM is shown by Eq. S3. The net radiation (R_n) of the soil-plant system is the difference of the incoming and outgoing shortwave (S_{in} and S_{out}, respectively) and longwave (L_{in} and L_{out}, respectively) radiation, i.e., the radiation absorbed by the soil-plant system. This absorbed radiation is available for sensible (H), latent (LE), ground heat flux (G) and storage (not included in this formulation). We assume one-dimensional (vertical), steady-state energy transport (no energy storage) common to many LSMs. The dynamics in model outputs are controlled by the change in the environmental forcing data. The steady-state simplification turns the solution from a numerical integration of a partial differential equation to a numerical solution of a set of nonlinear equations, allowing parallel computation.

$$R_n = S_{in} - S_{out} + L_{in} - L_{out} = H + LE + G \tag{S3}$$

The 'dual-source' and 'two-big-leaf' descriptors indicate how the overall energy balance is broken up into smaller components. The dual-source LSM structure means the surface is partitioned into plant canopy and ground components as sources of scalars (illustrated in Fig. S1). Additionally, we elect the two-layer form of the dual-source structure, similar to

CLM v5[2], where both canopy and soil interact with a canopy airspace (Fig. S1), which, in turn, interacts with the atmosphere above the canopy. The two-big-leaf approximation further partitions the canopy component into a sunlit and shaded big-leaf approximation, representing the integrated fluxes of all sunlit and shaded leaves. For clarity, actual leaf scale results are translated to the big leaf scale using the one-sided Leaf Area Index (LAI [$m^2\, leaf\, m^{-2}\, ground$]), which is further partitioned into sunlit and shaded LAI under the two-big-leaf approximation.

Before diving further into the energy balance of these LSM components, it is important to define some notation rules for the equations in this section that will clearly delineate the model structure. We have created five notation rules for our LSM structure. 1) A subscript of 'l' or 'g' indicates canopy/big-leaf or ground fluxes, respectively. 2) An additional subscript 'sl' or 'sh' following 'l' indicates the sunlit or shaded big leaf. respectively. 3) The index 'k', in lieu of 'sl' or 'sh', means the equation applies separately to both sunlit and shaded big leaves. 4) Shortwave radiation terms have an additional subscript 'par' or 'nir', identifying the specific radiation band, i.e., whether it is photosynthetically active radiation (PAR) or near infrared radiation (NIR). 5) The index 'Λ', in lieu of 'par' or 'nir', means the equation applies separately to both radiation bands.

Using the above conventions, Eq. S3 can then be further broken down into three smaller balances for the sunlit big leaf (Eq. S4), shaded big leaf (Eq. S5), and the soil/ground (Eq. S6). Balancing each of these equations separately is equivalent to balancing the overall energy budget in Eq. S3. Furthermore, each total flux (Eq. S3) requires consistency between model components as shown in Eq. S7-S10.

$$R_{n,l,sl} = S_{l,sl,par} + S_{l,sl,nir} + L_{l,sl} = H_{l,sl} + LE_{l,sl} \tag{S4}$$

$$R_{n,l,sh} = S_{l,sh,par} + S_{l,sh,nir} + L_{l,sh} = H_{l,sh} + LE_{l,sh} \tag{S5}$$

$$R_{n,g} = S_{g,par} + S_{g,nir} + L_g = H_g + LE_g + G_g \tag{S6}$$

$$R_n = R_{n,l,sl} + R_{n,l,sh} + R_{n,g} = R_{n,l,k} + R_{n,g} \tag{S7}$$

$$H = H_{l,sl} + H_{l,sh} + H_g = H_{l,k} + H_g \tag{S8}$$

$$LE = LE_{l,sl} + LE_{l,sh} + LE_g = LE_{l,k} + LE_g \tag{S9}$$

$$G = G_g \tag{S10}$$

S2.2 Radiative Transfer

The radiative transfer model was forced with incoming PAR, NIR and longwave radiation based on site measurements (see Sect. S5). Here we discuss the separate shortwave and longwave radiative transfer models.

S2.2.1 Shortwave Radiative Transfer

We use the Goudriaan and van Laar (GvL) model[3] to estimate shortwave radiative transfer in lieu of the two-stream approximation[2,4] used in CLM v5. Both approaches are two-stream models that focus on the upward and downward net fluxes of diffuse radiation with single scattering[5]. However, the GvL model yields simpler analytical forms and is used in other TBMs such as CABLE[6]. The reader is referred to Goudriaan and van Laar (1994)[3] or Bonan (2019)[5] for detailed derivation of the model. Shortwave radiation is partitioned into direct beam, scattered beam, and diffuse components of PAR and NIR. The two-big-leaf approximation also requires the assumption that shaded leaves only receive scattered beam and diffuse radiation, while sunlit leaves receive the same as well as direct beam radiation[2,5,7].

The total canopy shortwave radiation absorption $S_{l,\Lambda}$ is given by Eq. S11. This value must be partitioned appropriately between the sunlit and shaded big leaf. For ease of calculation and completeness, the sunlit leaf shortwave radiation absorption ($S_{l,sl,\Lambda}$, Eq. S12) is partitioned into direct beam ($S_{l,sl,\Lambda,b}$, Eq. S13), diffuse ($S_{l,sl,\Lambda,d}$, Eq. S14), and scattered direct beam ($S_{l,sl,\Lambda,sb}$, Eq. S15) components following De Pury and Farquhar (1997)[7]. The shaded leaf shortwave absorption ($S_{l,sh,\Lambda}$, Eq. S16) is simply the difference of total canopy absorption and sunlit leaf absorption, although analogous forms of the sunlit equations (Eq. S13-S15) can also be used[7].

$$S_{l,\Lambda} = \left(1-\rho'_{l,\Lambda,b}\right) S_{in,\Lambda,b} \left(1-\exp[-K'_{b,\Lambda}\cdot LAI]\right) + \left(1-\rho'_{l,\Lambda,d}\right) S_{in,\Lambda,d} \left(1-\exp[-K'_{d,\Lambda}\cdot LAI]\right) \tag{S11}$$

$$S_{l,sl,\Lambda} = S_{l,sl,\Lambda,b} + S_{l,sl,\Lambda,d} + S_{l,sl,\Lambda,sb} \tag{S12}$$

$$S_{l,sl,\Lambda,b} = S_{in,\Lambda,b}\cdot\alpha_{l,\Lambda}\cdot(1-\exp[-K_b\cdot LAI]) \tag{S13}$$

$$S_{l,sl,\Lambda,d} = S_{in,\Lambda,d}\cdot(1-\rho'_{l,\Lambda,d})\cdot(1-\exp[-(K'_{d,\Lambda}+K_b)\cdot LAI])\cdot\frac{K'_{d,\Lambda}}{K'_{d,\Lambda}+K_b} \tag{S14}$$

$$S_{l,sl,\Lambda,sb} = S_{in,\Lambda,b}\cdot((1-\rho'_{l,\Lambda,b})\cdot(1-\exp[-(K'_{b,\Lambda}+K_b)\cdot LAI])\cdot\frac{K'_{b,\Lambda}}{K'_{b,\Lambda}+K_b} + \alpha_{l,\Lambda}\cdot(1-\exp[-2K_b\cdot LAI])/2) \tag{S15}$$

$$S_{l,sh,\Lambda} = S_{l,\Lambda} - S_{l,sl,\Lambda} \tag{S16}$$

These shortwave radiative transfer equations rely on four essential parameters: the direct (K_b) and diffuse extinction coefficients (K_d) and the direct ($\rho'_{l,b}$) and diffuse canopy reflectance coefficients ($\rho'_{l,d}$). The K_b value is calculated by dividing the mean leaf angle ($G(Z)$) by the projection of sunlight onto a horizontal surface (Eq. S17), where Z is the sun zenith angle. The K_b value will change throughout the day as the sun moves across the sky since the angle of incidence with respect to leaf angles will vary. The function $G(Z)$ is known as the 'Ross-Goudriaan' function (Eq. S18-S20), which depends on a parameter, χ_l, that describes the leaf angle distribution's deviation from a spherical (i.e., random) distribution. As mentioned in Sect. S4, we calibrated χ_l to vary between -0.4 and 0.6.

$$K_b = \frac{G(Z)}{\cos(Z)} \tag{S17}$$

$$G(Z) = \phi_1 + \phi_2 \cos(Z) \tag{S18}$$

$$\phi_1 = 0.5 - 0.633\chi_l - 0.33\chi_l^2 \tag{S19}$$

$$\phi_2 = 0.877\,(1 - 2\phi_1) \tag{S20}$$

The diffuse radiation extinction coefficient, K_d, is calculated by integrating the direct beam transmissivity ($\tau_{l,b}$ shown in Eq. S21) over every solid angle of the hemisphere (Eq. S22) and then inverting the transmissivity law (Eq. S23). The transmissivity defines the percent of radiation that makes it through the canopy to the soil assuming exponential light extinction.

$$\tau_{l,b} = \exp\left(-K_b \cdot LAI\right) \tag{S21}$$

$$\tau_{l,d} = 2 \cdot \int_0^{\pi/2} \tau_{l,b} \cdot \cos Z \cdot \sin Z \, dZ \tag{S22}$$

$$K_d = \frac{-\ln \tau_{l,d}}{LAI} \tag{S23}$$

The GvL model has fewer equations than the CLM v5 two-stream approximation due to several simplifying assumptions. First, the single scattering of radiation can be accounted for in the extinction coefficients (K_b and K_d) simply by multiplying by the square root of leaf absorption (α_l)[3]. The extinction coefficients accounting for single-scattering are shown in Eq. S24-S25. Second, leaf transmissivity and reflectance are assumed identical—a reasonable assumption for green canopies[3]—allowing derivation of simplified relationships for direct beam ($\rho_{l,b}$, Eq. S26) and diffuse canopy reflectance ($\rho_{l,d}$, Eq. S27) based on idealized reflectance of horizontal leaves ($\rho_{l,h}$, Eq. S28). Readers are referred to Goudriaan (1977)[8] and Goudriaan and van Laar (1994)[3] for further details on these assumptions.

$$K'_{b,\Lambda} = \sqrt{\alpha_{l,\Lambda}} \cdot K_b \tag{S24}$$

$$K'_{d,\Lambda} = \sqrt{\alpha_{l,\Lambda}} \cdot K_d \tag{S25}$$

$$\rho_{l,b} = \frac{2K_b}{K_b + K_d} \rho_{l,h} \tag{S26}$$

$$\rho_{l,d} = \int_0^{\pi/2} 2 \cdot \rho_{l,b} \cdot \cos Z \cdot \sin Z \, dZ \tag{S27}$$

$$\rho_{l,h} = \frac{1 - \sqrt{\alpha_{l,\Lambda}}}{1 + \sqrt{\alpha_{l,\Lambda}}} \tag{S28}$$

The above canopy reflectance equations were derived for infinitely deep canopies. To account for the ground reflectance

(ρ_g), the approximations in Eq. S29-S30 are used. These approximations assume radiation travels through the canopy, reflects off the soil according to ρ_g, and travels back up through the canopy (hence the factor of 2 in the exponential term).

$$\rho'_{l,\Lambda,b} = \rho_{l,b} + \left(\rho_g - \rho_{l,b}\right) \cdot \exp(-2K'_b LAI) \tag{S29}$$

$$\rho'_{l,\Lambda,d} = \rho_{l,d} + \left(\rho_g - \rho_{l,b}\right) \cdot \exp(-2K'_d LAI) \tag{S30}$$

S2.2.2 Longwave Radiative Transfer

The longwave radiative transfer model follows the method laid out in Dai et al. (2004)[9], which is derived assuming exponential extinction of longwave radiation through the plant canopy. The net absorbed longwave radiation ($L_{l,k}$) is given by Eq. S31, which depends on the sunlit and shaded leaf temperature ($T_{l,k}$), ground temperature (T_g), fraction of longwave radiation absorbed by the canopy (δ_l, Eq. S32), the sunlit and shaded leaf fraction (F_k), and the Stefan-Boltzmann constant (σ). As mentioned previously, k is used to indicate that the equations are identical for sunlit or shaded big leaves.

$$L_{l,k} = \left(L_{in} - 2\sigma T_{l,k}^4 + \sigma T_g^4\right) \cdot \delta_l \cdot F_k \tag{S31}$$

$$\delta_l = 1 - \exp(-LAI) \tag{S32}$$

$$F_{k=1} = F_{sl} = \frac{1 - \exp(-K_b \cdot LAI)}{K_b \cdot LAI} \tag{S33}$$

$$F_{k=2} = F_{sh} = 1 - F_{sl} \tag{S34}$$

S2.3 Scalar Transport

Scalar transport for this LSM consists of prognostic equations for latent heat flux (LE), sensible heat flux (H) and gross primary productivity (GPP). The conserved quantities are mass of H_2O and CO_2 as well as enthalpy ($c_p \cdot T$). The states of the soil-plant system are given by partial pressure of H_2O (e), partial pressure of CO_2 (c) and temperature (T). First, we will describe the latent and sensible heat fluxes occurring between the canopy, ground, canopy airspace, and atmosphere. Then, we will elaborate on the coupled water vapor and CO_2 transport controlled by stomatal response to varying environmental conditions.

The two-layer approach[5] used in this LSM splits the transport equations into canopy, ground, and atmospheric fluxes that are coupled via the canopy airspace (shown in Fig. S1). In effect, there are four transport pathways: 1) sunlit canopy (big leaf) to canopy airspace, 2) shaded canopy (big leaf) to canopy airspace, 3) ground to canopy airspace, and 4) canopy airspace to atmosphere above canopy. The first three pathways must balance with the last pathway under the imposed steady-state conditions. All transport equations use integrated flux-gradient relationships (also known as conductance-difference relations or an analogy to Ohm's law) to calculate fluxes as the difference in potentials between two points in space multiplied by a conductance (inverse of resistance). As previously mentioned, the index k represents that an equation applies separately to both the sunlit and shaded big leaf, while their resultant states and fluxes will differ.

S2.3.1 Latent and Sensible Heat Fluxes

The transport of water vapor from the canopy to the canopy air space (transpiration) consists of two steps: 1) transport from the leaf mesophyll cells through the stomatal openings ($LE_{l,k}$, Eq. S35) and 2) transport through the laminar boundary layer at the leaf surface to the canopy air space (Eq. S36). The transpiration through the stomata is driven by a potential difference in the stomatal cavity vapor pressure ($e_{i,k}$) and the vapor pressure at the surface of the leaf ($e_{s,k}$) and mediated by the stomatal aperture controlled by stomatal conductance $g_{s,k}$. Likewise, the transport from the leaf surface to the canopy air space is driven by the difference in $e_{s,k}$ and vapor pressure in the canopy air space (e_{ca}) and mediated by the laminar boundary layer conductance to water vapor (g_{bv}). Since we assume steady state and use Ohm's analogy to represent transport, we can treat these two pathways as two resistors in series and calculate the overall transpiration from the canopy in a single equation (Eq. S37). Note that scaling from the individual leaf to the big-leaf approximation (i.e., canopy) is done simply by multiplying by the respective sunlit or shaded leaf area index (LAI_k). This assumes that all sunlit leaves have the same stomatal conductance and internal vapor pressure. Likewise, all shaded leaves have the same stomatal conductance and internal vapor pressure, which differs from the sunlit leaves. Additionally, we apply a mass-to-energy unit conversion (C_e) consisting of the latent heat of vaporization ($\mathscr{L}_v$), density of air (ρ_a), ratio of molar mass of water to molar mass of air (ε), and atmospheric pressure (P_{atm}). For simplicity, we have assumed a constant air density and have not modified it based on water vapor concentration or temperature. The *LE* equation is written assuming stomata on one side of the leaf as is common practice[5]. If a plant has stomata on both sides, it is usually accounted for in the stomatal conductance measurement and parameters.

$$LE_{l,k} = LAI_k \cdot C_e \cdot g_{s,k} \cdot \left(e_{i,k} - e_{s,k}\right) \tag{S35}$$

$$LE_{l,k} = LAI_k \cdot C_e \cdot g_{bv} \cdot \left(e_{s,k} - e_{ca}\right) \tag{S36}$$

$$LE_{l,k} = LAI_k \cdot C_e \cdot \frac{g_{s,k} \cdot g_{bv}}{g_{s,k} + g_{bv}} \cdot \left(e_{i,k} - e_{ca}\right) \tag{S37}$$

$$C_e = \frac{\mathscr{L}_v \cdot \rho_a \cdot \varepsilon}{P_{atm}} \tag{S38}$$

The description of sensible heat flux from the canopy is simpler than that of latent heat flux, as we assume no temperature gradient within a leaf. Therefore, heat transport is driven by temperature difference between the leaf ($T_{l,k}$) and canopy airspace (T_{ca}) only and mediated by the laminar boundary layer conductance to heat (g_{bh}). The result is scaled from a single leaf to the big-leaf approximation (i.e., canopy) by multiplying by the sunlit or shaded *LAI* as shown in Eq. S39. The underlying assumption here is that all sunlit leaves have one temperature and all shaded leaves have another at each time step. Furthermore, a conversion factor (C_h, Eq. S39) consisting of ρ_a and specific heat at constant pressure (c_p) is required to make the transport in terms of enthalpy which is the conserved quantity (not temperature). The factor of 2 in Eq. S39 represents transport from both sides of the leaf.

$$H_{l,k} = 2 \cdot LAI_k \cdot C_h \cdot g_{bh} \cdot \left(T_{l,k} - T_{ca}\right) \tag{S39}$$

$$C_h = \rho_a \cdot c_p \tag{S40}$$

There are four unknown conductances that must be calculated. The stomatal conductance g_s will be covered in the next section as it is coupled to carbon assimilation. The laminar boundary layer conductances for water vapor and heat are assumed identical based on Reynold's analogy[5] and are calculated using equations derived from heat transfer experiments on rigid steel leaves (Eq. S41). The calculation requires a turbulent transfer coefficient (C_l), a characteristic leaf dimension (d_l) and the friction velocity (u_*) measured at the flux tower.

$$g_{bv} = g_{bh} = \frac{C_l \cdot u_*}{d_l} \tag{S41}$$

Next, the transport of water and heat from the ground to the canopy airspace is shown in Eq. S42-S43. Much like $LE_{l,k}$, latent heat flux from the ground (LE_g) consists of two conductances in series driven by the vapor pressure difference in ground (e_g) and canopy airspace (e_{ca}). The conductances represent vapor transport through the tortuous soil pores when soil is not saturated (g_{sv}) and the subsequent transport from the soil surface to the canopy airspace through a laminar boundary layer (g'_{av}). The sensible heat flux from the ground to canopy airspace H_g is driven by the difference in ground temperature T_g and T_{ca} mediated by conductance of heat between soil surface and canopy airspace (g'_{ah}).

$$LE_g = C_e \cdot \frac{g_{sv} \cdot g'_{av}}{g_{sv} + g'_{av}} \cdot (e_g - e_{ca}) \tag{S42}$$

$$H_g = C_h \cdot g'_{ah} \cdot (T_g - T_{ca}) \tag{S43}$$

The conductance for both heat and water vapor from the soil are again assumed equivalent by Reynold's analogy and is calculated using a turbulent transfer coefficient (C_g) and u_* as assumed in Oleson et al. (2018)[2] (Eq. S44). The turbulent transfer coefficient is balanced between bare soil and dense canopy values using Eq. S45-S47. The reader is referred to Oleson et al. (2018)[2] and references therein for justification of these parametrizations.

$$g'_{av} = g'_{ah} = C_g \cdot u_* \tag{S44}$$

$$C_g = W \cdot C_{g,bare} + (1 - W) \cdot C_{g,dense} \tag{S45}$$

$$W = \exp(-LAI - SAI) \tag{S46}$$

$$C_{g,bare} = \frac{k}{0.13} \cdot \left(\frac{z_{om,g} \cdot u_*}{\nu}\right)^{-0.45} \tag{S47}$$

The additional conductance accounted for in unsaturated soils, g_{sv}, is calculated with Eq. S48 using an estimate of the dry soil layer (DSL), the water vapor diffusivity (D_v) and a shape factor describing the tortuosity of the soil pores (τ). The value of g_{sv} approaches ∞ as the soil becomes saturated to an incipient level (θ_i), which was calibrated in our analysis. If g_{sv} is infinite, the conductance in Eq. S42 simplifies to g'_{av}. The reader is again referred to Oleson et al. (2018)[2] and references therein for justification of these parametrizations.

$$g_{sv} = \frac{D_v \cdot \tau}{DSL} \tag{S48}$$

$$D_v = 2.12 \times 10^{-5} \cdot \left(\frac{T_g + 273.15}{273.15}\right)^{1.75} \tag{S49}$$

$$DSL = D_{max} \cdot \frac{\theta_i - \theta_s}{\theta_i - \theta_{air}} \tag{S50}$$

$$\tau = \phi_{air}^2 \cdot \left(\frac{\theta_{sat} - \theta_{air}}{\theta_{sat}}\right)^{3/b} \tag{S51}$$

Lastly, the latent and sensible heat fluxes from the canopy airspace to the atmosphere at the measurement point z are described in Eq. S52-S53. The potential differences are between vapor pressure and temperature in the canopy airspace (T_{ca} and e_{ca}) and the atmosphere at the flux tower measurement height (T_a and e_a). The conductance from the canopy airspace to the atmosphere is again the same for heat (g_{ah}) and vapor (g_{av}) by Reynold's analogy shown in Eq. S54. The conductance is based on the Monin-Obukhov similarity theory (MOST)[10], also known as the 'log-law'. The momentum roughness length (z_{om}), heat/vapor roughness length (z_{oh}), and zero-plane displacement height (d_o) are empirical parameters. The z_{om} was determined from literature while the other two parameters are calculated using practical relationships[11] (Eq. S55-S56). For this study, we neglected the impact of atmospheric stability on the atmospheric conductance term. These effects are usually handled by correction factors accounting for how density stratifications in the atmosphere enhance or suppress turbulent transport. However, the stability corrections add another level of complexity to the numerical scheme, as they are dependent on H and LE, and are not important to the overall question of this research.

$$LE = C_e \cdot g_{av} \cdot (e_{ca} - e_a) \tag{S52}$$

$$H = C_h \cdot g_{ah} \cdot (T_{ca} - T_a) \tag{S53}$$

$$g_{ah} = g_{av} = \frac{\overline{u} \cdot k^2}{\ln\left(\frac{z_m - d_o}{z_{om}}\right) \cdot \ln\left(\frac{z_m - d_o}{z_{oh}}\right)} \tag{S54}$$

$$z_{oh} = 0.1 \cdot z_{om} \tag{S55}$$

$$d_o = 0.7 \cdot h \tag{S56}$$

In summary, Eq. S35-S56 contain five prognostic variables: $T_{l,sl}$, $T_{l,sh}$, T_g, $g_{s,sl}$, and $g_{s,sh}$. An important assumption for scalar transport is that the vapor pressures $e_{i,k}$ and e_g are assumed to be dependent on $T_{l,k}$ and T_g via the Clausius-Clapeyron relationship[5]. Furthermore, the states of the canopy airspace, e_{ca} and T_{ca}, are completely determined by the states and conductances of the canopy, ground, and atmosphere. Substituting Eq. S37, S39, S42, S43, S52 and S53 into Eq. S8-S9 and solving for e_{ca} and T_{ca} yields weighted averages of the other conductances and states (Eq. S57-S58). All other terms in the scalar transport equations are either forcing data, parameters, or constants. Therefore, we have at least five variables thus far that must be solved for.

$$e_{ca} = \frac{g_{av} \cdot e_a + g_{l,sl} \cdot e_{i,sl} + g_{l,sh} \cdot e_{i,sh} + g_{av,g} \cdot e_g}{g_{av} + g_{l,sl} + g_{l,sh} + g_{av,g}} \tag{S57}$$

$$T_{ca} = \frac{g_{ah} \cdot T_a + g_{bh} \cdot T_{l,sl} + g_{bh} \cdot T_{l,sh} + g_{ah,g} \cdot T_g}{g_{ah} + 2 \cdot g_{bh} + g_{ah,g}} \tag{S58}$$

$$g_{l,k} = \frac{LAI_k \cdot g_{s,k} \cdot g_{bv}}{g_{s,k} + g_{bv}} \tag{S59}$$

S2.4 Stomatal Conductance and CO_2 Assimilation

Stomatal conductance (g_s) is intrinsically tied to CO_2 assimilation as stomatal aperture and CO_2 gradient controls photosynthetic carbon fixation. We utilize a steady state, coupled stomatal conductance-photosynthesis scheme similar to Oleson et al. (2013)[12] that balances CO_2 assimilation with CO_2 diffusion into the leaf. Specifically, we utilize the Medlyn stomatal conductance model[13] to represent stomatal responses to atmospheric conditions coupled with the Farquhar, von Caemmerer, and Berry (1980) C3 photosynthesis model[14] (hereafter, referred to as FvCB model).

S2.4.1 Medlyn Stomatal Conductance Model

We estimate the well-watered stomatal conductance ($g_{s,ww,k}$), i.e., stomatal conductance without stomatal closure due to water transport from soil to leaf, using the Medlyn optimality model[13] (Eq. S60). The Medlyn model assumes plants adjust stomatal aperture in order to minimize the water lost by transpiration for a certain carbon gain at each instant under light-limited photosynthetic conditions (although it is also commonly used to describe stomatal behavior during Rubisco-limited conditions). The solution of a resulting calculus of variations problem yields a relation where stomata close under higher vapor pressure deficit ($D_k = e_{i,k} - e_{s,k}$) and leaf surface CO_2 concentration (c_s), and open with higher CO_2 assimilation ($A_{n,k}$). This model provided a unifying framework for previously successful empirical methods[15] and is parametrized by the minimum stomatal conductance (g_o) and a species-specific slope parameter (g_1) related to the marginal carbon gain to water loss.

$$g_{s,ww,k} = g_o + \left(1 + \frac{g_1}{\sqrt{D^k/10^3}}\right) \frac{1.6 \cdot A_{n,k}}{(c_s/P_{atm}) \cdot 10^6} \tag{S60}$$

The Medlyn equation provides a link between CO_2 diffusion into the leaf ($A^d_{n,k}$) and CO_2 assimilation determined by a photosynthetic model ($A_{n,k}$). The CO_2 diffusive transport equation (Eq. S61) contains $g_{s,k}$, which is simply the well-watered Medlyn value $g_{s,ww,k}$ reduced by a chosen transpiration downregulation scheme discussed in Sect. S2.5. (Note: CO_2 transport into the leaf via diffusion is nearly identical to that of water vapor (Eq. S37), with increases to stomatal and laminar boundary layer conductances of 1.6 and 1.4, respectively, to account for the differing diffusivities of CO_2 compared to H_2O.) The CO_2 assimilation through photosynthesis appears as the term $A_{n,k}$ in Eq. S60. Our LSM solution scheme (Sect. S2.6) ensures that diffusive CO_2 transport into the leaf is balance by CO_2 assimilation, i.e., $A^d_{n,k} = A_{n,k}$.

$$A^d_{n,k} = \frac{g_{s,k} \cdot g_{bv}}{1.4 g_{s,k} + 1.6 g_{bv}} \cdot \frac{\left(c_{i,k} - c_{ca}\right)}{P_{atm}} \cdot 10^6 \tag{S61}$$

S2.4.2 FvCB C3 Photosynthesis Model

The FcVB model[14] represents the three limiting mechanisms of the Calvin Cycle for steady-state carbon assimilation from atmospheric CO_2: 1) the enzyme kinetics of Ribulose 1,5 bisphosphate carboxylase-oxyganese (Rubisco), 2) the Ribulose 1,5 bisphosphate (RuBP) regeneration rate governed by ATP and NADPH created in the election transport chain of the light reactions, and 3) the amount of triose phosphates (starches) a plant can use. The equations here are for C3 photosynthesis only following Oleson et al. (2018)[2].

Rubisco-limitation is represented using Michaelis-Menten (MM) kinetics that describe uptake velocity of a fixed amount of Rubisco when RuBP is saturated at an internal concentration of CO_2 (Eq. S62). The equation determines the amount of CO_2 assimilated or released depending on whether Rubisco combines RuBP with CO_2 (carboxylation) or RuBP with O_2 (oxygenation). Thus, the equation requires values for partial pressure of oxygen in the leaf (o_i, Eq. S63), MM constant for CO_2 (K_c, Eq. S64), MM constant for O_2 (K_o, Eq. S65), and the CO_2 compensation point (Γ, Eq. S66).

$$A_{c,k} = V_{max25} \frac{c_{i,k} - \Gamma}{c_{i,k} + K_c \left(1 + o_i / K_o\right)} \quad \text{(S62)}$$

$$o_i = 0.209 \cdot P_{atm} \quad \text{(S63)}$$

$$K_c = 404.9 \times 10^{-6} \cdot P_{atm} \quad \text{(S64)}$$

$$K_o = 278.4 \times 10^{-3} \cdot P_{atm} \quad \text{(S65)}$$

$$\Gamma = 42.75 \times 10^{-6} \cdot P_{atm} \quad \text{(S66)}$$

The RuBP-limited assimilation rate (A_j, Eq. S67), also known as the light-limited rate, describes conditions where the RuBP is limiting due to shortages in NADPH and ATP from the electron transport chain in the thykaloid of the mesophyll cells. A balance of the number of electrons required to create the required NADPH for RuBP regneration yields Eq. S67 where the rate of electron transport (J) is a key quantity. The electron transport rate is itself co-limited between a maximum rate (J_{max25}) and the efficiency of photosystem II at delivering electrons (I_{PSII}, Eq. S68) from the absorbed PAR by the leaf ($S_{l,k,par}$). The factor of 4.6 in Eq. S68 represents unit conversion from joules to μmoles of photons[16]. The quantum efficiency of photosystem II (Φ_{PSII}) is usually taken to be 0.7 μmoles of electrons per μmoles of photons[2].

$$A_{j,k} = J \frac{c_{i,k} - \Gamma}{4c_{i,k} + 8\Gamma} \quad \text{(S67)}$$

$$I_{PSII,k} = 0.5 \cdot \Phi_{PSII} \cdot \left(4.6 \cdot S_{l,k,par}\right) \quad \text{(S68)}$$

$$\Theta_{PSII} \cdot J^2 - (I_{PSII,k} + J_{max25}) \cdot J + I_{PSII,k} \cdot J_{max25} = 0 \quad \text{(S69)}$$

The product-limited assimilation rate (A_p, Eq. S70) represents the upper limit on assimilation based on the plant's need for the starches. See Oleson et al. (2018)[2] and sources within for justifications of the relationship with V_{max25}.

$$A_p = V_{max25}/6 \quad \text{(S70)}$$

Altogether, we want to calculate the co-limitation of these three controls on plant CO_2 assimilation. To do this, we use quadratic equations to estimate the co-limitation as laid out in Collatz et al. (1991)[17] to allow a gradual transition across the three mechanisms and to account for joint effects of the three limits. The Θ_{cj} and Θ_{ip} are empirical curvature factors that control for this gradual transition[2]. The overall CO_2 assimilation A_k is given by the root of Eq. S71 and S72. Lastly, we must remove from A_k the amount of CO_2 that is released through dark respiration R_d to get the overall net assimilation $A_{n,k}$ (Eq. S73). $A_{n,k}$ is the amount of CO_2 assimilated from the atmosphere, which we balance with CO_2 diffusion into the leaf ($A^d_{n,k}$; Eq. S58).

$$\Theta_{cj} \cdot A_{i,k}^2 - (A_{c,k}+A_{j,k}) \cdot A_{i,k} + A_{c,k} \cdot A_{j,k} = 0 \quad \text{(S71)}$$

$$\Theta_{ip} \cdot A_k^2 - (A_{i,k}+A_{p,k}) \cdot A_k + A_{i,k} \cdot A_{p,k} = 0 \quad \text{(S72)}$$

$$A_{n,k} = A_k - R_d \quad \text{(S73)}$$

$$R_d = 0.015 \cdot V_{max25} \quad \text{(S74)}$$

For simplicity, we have omitted the temperature dependence of the photosynthetic parameters V_{max25}, J_{max25}, R_d, K_c, K_o, and Γ and simply use the values at 25^oC[18–20]. These dependencies are typically handled with Arrhenius functions[5] to account for the breakdown or acceleration of various metabolic processes at high and low temperatures. Since the goal of this paper was to test the transpiration downregulation schemes, we omitted the temperature dependence due to the need for many more parameters to properly use the Arrhenius functions. We do not believe this simplification would alter the main conclusions on the differences between β and PHMs because both models incur the same errors by neglecting temperature dependence.

S2.4.3 Scale Correction of Photosynthetic Parameters

The maximum carboxylation rate of the Rubisco enzyme (V_{max25}) and the maximum electron transport rate (J_{max25}) are dependent on nitrogen availability in the leaf. Nitrogen content has been been found to exponentially decay with relative cumulative leaf area in the canopy[21]; therefore, both V_{max25} and J_{max25} vary nonlinearly with distance from the top of the canopy. For simplicity, we use methods from De Pury and Farquhar (1997)[7] and Dai et al. (2004)[9] to scale V_{max25} and J_{max25}, respectively, which accounts for this nonlinear nitrogen profile by integrating these rates through the canopy to get a single, effective value. These methods differ from the optimality principles used in CLM v5[2].

The overall Rubisco carboxylation capacity of the canopy ($V_{l,max25}$) factoring in leaf nitrogen is given Eq. S75, where K_n is the extinction coefficient for leaf nitrogen content. The two-big-leaf model requires separate consideration of the sunlit and shaded big leaf[22] shown in Eq. S76-S77. The maximum electron transport rate of the canopy ($J_{l,max25}$) factoring in leaf nitrogen is given in Eq. S78, while the sunlit and shaded big leaf values are shown in Eq. S79-S80. The values of $V_{l,k,max25}$ and $J_{l,k,max25}$ are used in place of the V_{max25} and J_{max25} parameters for the FvCB model described in the previous section. Note, the scaled photosynthetic parameters do change at each timestep because the sun moving across the sky changes the fraction of sunlit and shaded leaves and, in turn, the integrated rate parameters.

$$V_{l,max25} = LAI \cdot V_{max25} \cdot [1 - \exp(-K_n)] \tag{S75}$$

$$V_{l,sl,max25} = LAI \cdot V_{max} \cdot \frac{1 - \exp(-K_n - K_b \cdot LAI)}{K_n + K_b \cdot LAI} \tag{S76}$$

$$V_{l,sh,max25} = V_{l,max25} - V_{l,sl,max25} \tag{S77}$$

$$J_{l,max25} = J_{max25} \cdot \frac{1 - \exp\left(-K'_d \cdot LAI\right)}{K'_d} \tag{S78}$$

$$J_{l,sl,max25} = J_{max25} \cdot \frac{1 - \exp\left(-[K'_d + K_b] \cdot LAI\right)}{K'_d + K_b} \tag{S79}$$

$$J_{l,sh,max25} = J_{l,max25} - J_{l,sl,max25} \tag{S80}$$

S2.5 Transpiration Downregulation

The transpiration downregulation schemes used in the main article are the empirical β and Plant Hydraulic Model schemes (PHM). We will discuss how each is implemented to suppress transpiration under soil water stress. The reader is referred to the main article for detailed discussion on the theoretical justification for the two methods.

S2.5.1 Well-Watered Transpiration

Before discussing the transpiration downregulation schemes, we must first clarify the terminology 'well-watered'. As stated in the main article, well-watered refers to soil water conditions that do not cause any limitation to transpiration through stomatal closure via low leaf water potential. In other words, the transpiration meets the stomata-regulated atmospheric moisture demand—determined by the Medlyn model (Eq. S60) and the driving vapor pressure difference. This definition becomes slightly more ambiguous as we introduce a dual-source, two-big-leaf model structure, as the states (vapor pressure and temperature) experienced by the hypothetical big leaves at a time step adjust to downregulation. Therefore, for clarity, the well-watered transpiration rate corresponds to the states calculated when transpiration downregulation is turned off, i.e., representing no soil water stress. This approach differs from CLM v5[2], which considers well-watered transpiration to be the rate under the downregulated states. This distinction between the two definitions of the well-watered rate will become important shortly, as the well-watered rate is a key variable in the transpiration downregulation schemes. Also, note that the well-watered rate is different between sunlit and shaded big leaf as they encounter differing temperatures, light, and vapor pressures.

S2.5.2 β Downregulation Schemes

As mentioned in the main article, the LSM utilizes a Weibull function to represent the empirical β curve (Eq. 13 in the main article). There are three variants of this method used: 1) a single β, 2) a 2-leaf β, and 3) a dynamic β. Since the method is empirical, there is not firm guidance on where within the plant to apply this downregulation, as some models apply it directly to well-watered stomatal conductance and other apply it to photosynthetic parameters like V_{max25}. Here, we apply β to the well-watered transpiration rate of the sunlit and shaded big leaf to maintain consistency with our minimalist analysis. Sect.

S2.6.1 will discuss in greater detail how β is applied.

S2.5.3 PHM Downregulation Scheme

We will elaborate here on the PHM laid out in the main article and extend its formulation to the two-big leaf approach of the LSM. The PHM describes one-dimensional water transport through the soil-plant system and is similar to that in CLM v5[2,23]. However, we have simplified the segmentation to soil-to-xylem, xylem-to-leaf, and leaf-to atmosphere compartments. For readability the equations shown in the main article are repeated here. Each segment has a conductance curve that downregulates from the maximum conductance values based on water potentials through the segment. The conductivity equations follow closely the work of Manzoni et al. (2014)[24] and Feng et al. (2018)[25] and references therein. All parameter values and units for the following equations can be found in Table S4.

The soil-to-xylem conductance (g_{sx}, Eq. S81) consists of the well-known unsaturated hydraulic conductivity curve for soil[26] and a maximum conductance value ($g_{sx,max}$, Eq. S82). The downregulation function is parametrized by saturated soil water potential (ψ_{sat}), soil water retention exponent (b), unsaturated hydraulic conductivity exponent ($c = 2b+3$), and a correction factor (d) to account for roots' ability to reach water[27]. During the calibration process (Sect. S4), we found that $d = 0$ to obtain realistic soil parameters, but it is included in our formulation for completeness. The $g_{sx,max}$ value is calculated using the saturated hydraulic conductivity ($k_{s,sat}$), specific weight of water ($\rho_w \cdot g$) and a length scale based on root area index (RAI), fine root diameter (d_r) and effective rooting depth (Z_r) to convert to conductance. We assume a single, homogeneous soil layer described by a constant water characteristic curve, average transport distance to root, and a root zone soil water potential (ψ_s).

$$g_{sx}(\psi) = g_{sx,max} \cdot \left(\frac{\psi_{sat}}{\psi}\right)^{\frac{c-d}{b}} \tag{S81}$$

$$g_{sx,max} = \frac{k_{s,sat}}{\rho_w \cdot g} \cdot \sqrt{\frac{RAI}{d_R \cdot Z_r}} \cdot 10^{-6} \tag{S82}$$

The xylem-to-leaf conductance, g_{xl} (Eq. S83), is the maximum xylem-to-leaf conductance ($g_{xl,max}$, Eq. S83) downregulated by a sigmoidal function[28] parametrized by the vulnerability exponent a and the xylem water potential (ψ_x) at 50% loss of conductance ($\psi_{x,50}$) due to xylem embolism. The $g_{xl,max}$ is estimated using sapwood-specific hydraulic conductivity (K_{sap}), the sapwood area index ($SapAI$) and the height of vegetation (h_v), which assumes uniform conductivity and sapwood area through the plant.

$$g_{xl}(\psi) = g_{xl,max} \cdot \left[1 - \frac{1}{1 + e^{a \cdot (\psi - \psi_{x,50})}}\right] \tag{S83}$$

$$g_{xl,max} = \frac{K_{sap} \cdot SapAI}{h_v \cdot \rho_w} \tag{S84}$$

The leaf-to-atmosphere conductance (Eq. S85) is the stomatal conductance for the sunlit and shaded leaf, $g_{s,k}$, downregulated from its well-watered value ($g_{s,ww,k}$) using a Weibull function parametrized by a shape factor (b_l) describing stomatal sensitivity and the leaf water potential at 50% loss of conductance ($\psi_{l,50}$)[29]. The $g_{s,ww,k}$ value is calculated using the Medlyn model previously discussed in Eq. S60[13]. The values for stomatal conductance are defined for both sunlit and shaded leaf by index k as they will almost always differ.

$$g_{s,k} = g_{s,ww,k} \cdot 2^{-\left(\frac{\psi_{l,k}}{\psi_{l,50}}\right)^{b_l}} \tag{S85}$$

In order to calculate the water flux through each segment, we must utilize a Kirchhoff transform (Eq. S86) to account for the the varying potential (and conductance) along each segment[30]. The transform is only performed on the soil-to-xylem and xylem-to-leaf segments as the distance traveled through the leaf to stomata is assumed negligible. The total flux potential for soil-to-xylem ($\Phi_{sx}(\psi)$, Eq. S87) and xylem-to-leaf ($\Phi_{xl}(\psi)$, Eq. S88) give an upper limit on the water that could be extracted from a segment based on the potential. Using this linearized flow theory, the flux through each segment is simply calculated by taking the difference in total flux potential between the end points of each segment.

$$\Phi(\psi) = \int_{-\infty}^{\psi} K\left(\psi'\right) d\psi' \tag{S86}$$

$$\Phi_{sx}(\psi) = \frac{b \cdot g_{sx,max} \cdot \psi}{b-c+d} \cdot \left(\frac{\psi_{sat}}{\psi}\right)^{\frac{c-d}{b}} \tag{S87}$$

$$\Phi_{xl}(\psi) = g_{xl,max} \cdot \left[\frac{\ln\left(e^{-a\cdot\psi} + e^{-a\cdot\psi_{50}}\right)}{a} + \psi\right] \tag{S88}$$

The two-big leaf configuration of this model requires five total segments: soil-to-xylem, xylem-to-sunlit leaf, xylem-to-shaded leaf, sunlit leaf-to-atmosphere, and shaded leaf-to-atmosphere. The underlying assumption is that the transport from xylem to the sunlit and shaded leaf is completely independent. The transport in each segment is shown below in Eq. S89-S91. Note these equations are the same as Equations 9-11 in the main article except adapted for the two-big-leaf configuration.

$$LE_{sx} = \left[\Phi_{sx}(\psi_s) - \Phi_{sx}(\psi_x)\right] \cdot \rho_w \cdot \mathscr{L}_v \tag{S89}$$

$$LE_{xl,k} = \left[\Phi_{xl}(\psi_x) - \Phi_{xl}(\psi_{l,k})\right] \cdot \rho_w \cdot \mathscr{L}_v \tag{S90}$$

$$LE_{la,k} = LAI_k \cdot g_{s,k} \cdot \left(e_{i,k} - e_{s,k}\right) \cdot C_e \tag{S91}$$

We assume a steady-state solution where the supply through the soil-plant system equals the atmospheric moisture demand. This problem can be solved using a Newton-Raphson method as done in CLM v5[2]. However, this method was found to be unstable under certain conditions; therefore, we opted to use nonlinear least squares in MATLAB (*lsqnonlin*) to solve the problem. We used the Levenberg-Marquardt scheme, which is an unconstrained, quasi-Newton optimization routine. The optimization problem is laid out in Eq. S92-S94. The xylem, sunlit leaf, and shaded leaf water potentials are the decision variables (ψ, Eq. S94) that attempt to minimize the residuals (R, Eq. S93) that represent flow differences between connected segments. Therefore, when the residual vector becomes 0, flow is balanced through all segments and we have obtained our steady-state solution. We explored using constrained optimization (as in Sect. S2.6) for this problem, but it did not appear to provide any additional benefit and took longer to solve.

$$\psi^* = \min_{\psi} \quad \|R\|^2 \tag{S92}$$

$$R = \begin{bmatrix} LE_{sx} - \sum_{k=1}^{2} LE_{xl,k} \\ LE_{xl,sl} - LE_{la,sl} \\ LE_{xl,sh} - LE_{la,sh} \end{bmatrix} \tag{S93}$$

$$\psi = \begin{bmatrix} \psi_{l,sl} \\ \psi_{l,sh} \\ \psi_x \end{bmatrix} \tag{S94}$$

S2.6 LSM Solution Scheme

There are numerous ways to solve the steady-state dual-source scheme depending on how the equations and unknowns have been defined. Here, we have created our own method, similar to CLM v5. There are two overall computational schemes or solvers: a well-watered solver and a transpiration downregulation solver. In the well-watered solver, there are two levels of computation: the surface energy budget solver (outer solver) and the scalar transport solver (inner solver). For the transpiration downregulation scheme, well-watered solutions are adjusted in a separate solver based on soil moisture availability. Our solvers use optimization routines rather than the Newton-Raphson methods used in CLM v5 for several reasons: 1) numerical derivatives are required for both methods, 2) the optimization routine guards against solution divergence, 3) the optimization routine is simple to set up, and 4) speed between the two methods at our scale is essentially the same.

S2.6.1 Well-Watered Solver

The well-watered solver is the primary solution scheme of the LSM, which is run for every simulation with and without transpiration downregulation. The solver consists of two nested least squares optimization problems, which have been referred to as the outer and inner solvers for simplicity. There are six overall state variables that must be adjusted to balance the surface energy budget (Eq. S3) for this steady-state problem: $T_{l,k}$, T_g, $c_{i,k}$ and e_{ca}. The outer solver is concerned with balancing the surface energy budget by finding the correct leaf ($T_{l,k}$) and ground (T_g) temperatures, whereas the inner solver is focused on finding the correct internal leaf carbon concentrations ($c_{i,k}$) and canopy water vapor pressure (e_{ca}) that balance the LE and H leaving the ground and canopy with the transport from the canopy airspace to atmosphere.

The outer solver is a three dimensional nonlinear least squares problem shown in Eq. S95-S97. The residuals being minimized (R^o) are the sunlit big leaf, shaded big leaf, and ground energy balances in Eq. S4-S6, while the decision variables (T) are the temperatures of these three respective compartments. The outer solver is illustrated in (Fig. S2) as it begins by gathering all the environmental forcing data for a particular time step (Sect. S5). The outer solver then initiates a guess for the three temperatures based on the air temperature. The next step is to solve the GvL radiative transfer model to obtain the net radiation R_n for the three compartments and their breakdown into PAR, NIR, and longwave components. At this point, the temperatures are sent to the inner solver to determine the scalar fluxes from the ground, canopy, and canopy airspace under these fixed temperatures and states. Once the inner solver finds the $c_{i,k}$ and e_{ca} that balances Eq. S8-S9, the scalar fluxes for all compartments are calculated. The outer solver then checks to see if the net radiation in each compartment equals the scalar fluxes. If not, the temperatures are adjusted based on the optimization routine and the process is repeated until convergence.

$$
\begin{aligned}
T^* = \min_{T} \quad & \|R^o\|^2 \\
\text{s.t.} \quad & T \in (0, 40)
\end{aligned} \tag{S95}
$$

$$
R^o = \begin{bmatrix} S_{l,sl,par} + S_{l,sl,nir} + L_{l,sl} - H_{l,sl} - LE_{l,sl} \\ S_{l,sh,par} + S_{l,sh,nir} + L_{l,sh} - H_{l,sh} - LE_{l,sh} \\ S_{g,par} + S_{g,nir} + L_g - H_g - LE_g - G_g \end{bmatrix} \tag{S96}
$$

$$
T = \begin{bmatrix} T_{l,sl} \\ T_{l,sh} \\ T_g \end{bmatrix} \tag{S97}
$$

The inner solver is also a three dimensional nonlinear least squares problem within the outer solver shown in Eq. S98-S100. The inner solver is given temperatures and states of the two big leaves, ground, and air and must find the internal CO_2 concentrations that balance plant carbon assimilation with leaf diffusion as well as the canopy airspace water vapor pressure that balances scalar transport from ground and canopy with that to the atmosphere. The inner solver is shown in Fig. S2 as the light gray indented panels. First, values of $c_{i,k}$ and e_{ca} are guessed based on atmospheric conditions. Then the FvCB model is solved to calculate the net CO_2 assimilation of each leaf ($A_{n,k}$), which must the diffusive CO_2 flux into the leaf $A^d_{n,k}$. A neat trick introduced in CLM v5[2] is to substitute the diffusion equation (Eq. S61) into the Medlyn equation (Eq. S60) to obtain a quadratic equation whose larger root is the solution for $g_{s,k}$ (Eq. S101-S103). Using $g_{s,k}$, the internal carbon concentration from leaf diffusion ($c^+_{i,k}$) is calculated and checked against the assumed value of the solver $c_{i,k}$. Once $g_{s,k}$ has been determined, we can use Eq. S57 to calculate a check on the canopy airspace water vapor pressure (e^+_{ca}). These values are adjusted by the optimization routine until convergence criteria is met. The results are then sent back out to the outer solver.

$$x^* = \min_{x} \quad \|R^i\|^2 \tag{S98}$$
$$\text{s.t.} \quad x \in (0, 40)$$

$$R^i = \begin{bmatrix} c^+_{i,sl} - c_{i,sl} \\ c^+_{i,sh} - c_{i,sh} \\ e^+_{ca} - e_{ca} \end{bmatrix} \tag{S99}$$

$$x = \begin{bmatrix} c_{i,sl} \\ c_{i,sh} \\ e_{ca} \end{bmatrix} \tag{S100}$$

$$g_{s,j}^2 - \left[2 \cdot g_o + 2 \cdot C_{1,j} + \frac{C_{1,j}^2 \cdot g_1^2}{g_{bv} \cdot C_{2,j}}\right] g_{s,j} + \left[g_o^2 + 2 \cdot C_{1,j} \cdot g_o + C_{1,j}^2 \left(1 - \frac{g_1^2}{C_{2,j}}\right)\right] = 0 \tag{S101}$$

$$C_{1,j} = \frac{1.6 \cdot A_{n,j} \cdot P_{atm}}{c_{s,j} \cdot 10^6} \tag{S102}$$

$$C_{2,j} = \frac{e_{i,j} - e_{ca}}{1000} \tag{S103}$$

S2.6.2 Transpiration Downregulation Solver

The transpiration downregulation solver is an additional solver used after the well-watered solver to account for the effect of soil water stress on stomatal conductance and, in turn, on the scalar fluxes and plant microclimate. The solver scheme is a single least squares problem (Eq. S104) in five dimensions of leaf temperatures and conductances as well as ground temperature (Eq. S106). As in the well-watered solver, the first three residuals are the surface energy balance for the big leaves and ground (Eq. S105). The final two residuals (Eq. S107) ensure that the transpriation from the canopy calculated by the scalar transport module match the value calculated by the selected downregulation method; either β or PHM. For the β method, the downregulated transpiration is simply β multiplied by the well-watered transpriation rate $LE_{l,k,ww}$. For the the PHM method, the downregulated transpiration rate ($LE_{l,k,phm}$) is the solution to the PHM that balances supply and demand (Eq. S92-S94).

The solver scheme is laid out in Fig. S3 where it initializes the five decision variables from the well-watered solution. For the set temperatures and conductances we are able to re-calculate the longwave radiation, carbon assimilation, scalar fluxes and states. At this point, we can calculate the the surface energy budget residuals in Eq. S105. Now there is a choice to make whether to select the β model or the PHM. The β model is less computationally expensive as we simply multiply β by the already calculated $LE_{l,k,ww}$. Any of the three β methods (β_s, β_{2L}, and β_{dyn}) can be applied at this point as there is no real computational difference between the three, just different β values are multiplied by the well-watered rates. The PHM scheme is slightly more complex as we must solve the three-dimensional least squares problem to balance supply and demand (Sect. S2.5.2). However, both schemes then check the last two residuals (Eq. S107) to ensure the transpiration from the scalar transport module (Eq. S37) match the downregulation scheme transpiration. If the residual does not converge the solver adjusts the decision variable and repeats.

This transpiration downregulation scheme is different than that proposed by CLM v5[2] not only numerically but also in how the well-watered transpiration is defined. As seen in our scheme (Fig. S3), our well-watered transpiration is fixed. We opted for this because the states of the plant microclimate under well-watered conditions are different then under downregulation. Therefore, under the same atmospheric forcings our method is consistent with what we would expect to see if the soil was saturated compared to when it is dry. The method in CLM v5 continually updates the well-watered transpiration during the downregulation solver. Essentially, as the microclimate states change during downregulation, CLM v5 re-calculates the well-watered stomatal conductance according to the Medlyn model and uses that in the downregulation schemes. This creates a positive feedback that increases transpiration suppression compared to our method. Also, the well-watered transpiration rate calculated in this method is the value that would be experienced in a certain plant microclimate and not necessarily under the atmospheric forcings. It is difficult to determine which method is most realistic, but they give very different values for downregulation. We think our definition of well-watered transpiration is more appropriate to defining the stomata-regulated atmospheric moisture demand so that is what was used in this analysis.

$$x^* = \min_x \quad \|R^t\|^2 \qquad \text{s.t.} \quad x \in (0,40) \tag{S104}$$

$$R^t = \begin{bmatrix} S_{l,sl,par} + S_{l,sl,nir} + L_{l,sl} - H_{l,sl} - LE_{l,sl} \\ S_{l,sh,par} + S_{l,sh,nir} + L_{l,sh} - H_{l,sh} - LE_{l,sh} \\ S_{g,par} + S_{g,nir} + L_g - H_g - LE_g - G_g \\ R^t_{(4)} \\ R^t_{(5)} \end{bmatrix} \tag{S105}$$

$$x = \begin{bmatrix} T_{l,sl} \\ T_{l,sh} \\ T_g \\ g_{l,sl} \\ g_{l,sh} \end{bmatrix} \tag{S106}$$

$$R^t_{(4,5)} = \begin{cases} LE_{l,k,phm} - LE_{l,sl} & \text{if PHM scheme} \\ LE_{l,k} - \beta \cdot LE_{l,k,ww} & \text{if } \beta \text{ scheme} \end{cases} \tag{S107}$$

Surface Energy Budget

$R_n = S_{in} - S_{out} + L_{in} - L_{out} = H + LE + G$

Radiation Model: Goudriaan and Van Laar (1994)

Photosynthesis Model: Farquhar (1980)

Plant Hydraulics Model: Similar to Manzoni (2013)

Model Structure: Dual source, 2-Big Leaf Approximation

Model Forced With

- Vapor Pressure Defecit
- Air Temperature
- Soil Moisture
- Ground Heat Flux
- Streamwise Velocity
- Incoming Shortwave Radiation
- Incoming Longwave Radiation
- CO_2 Concentration
- Air Pressure

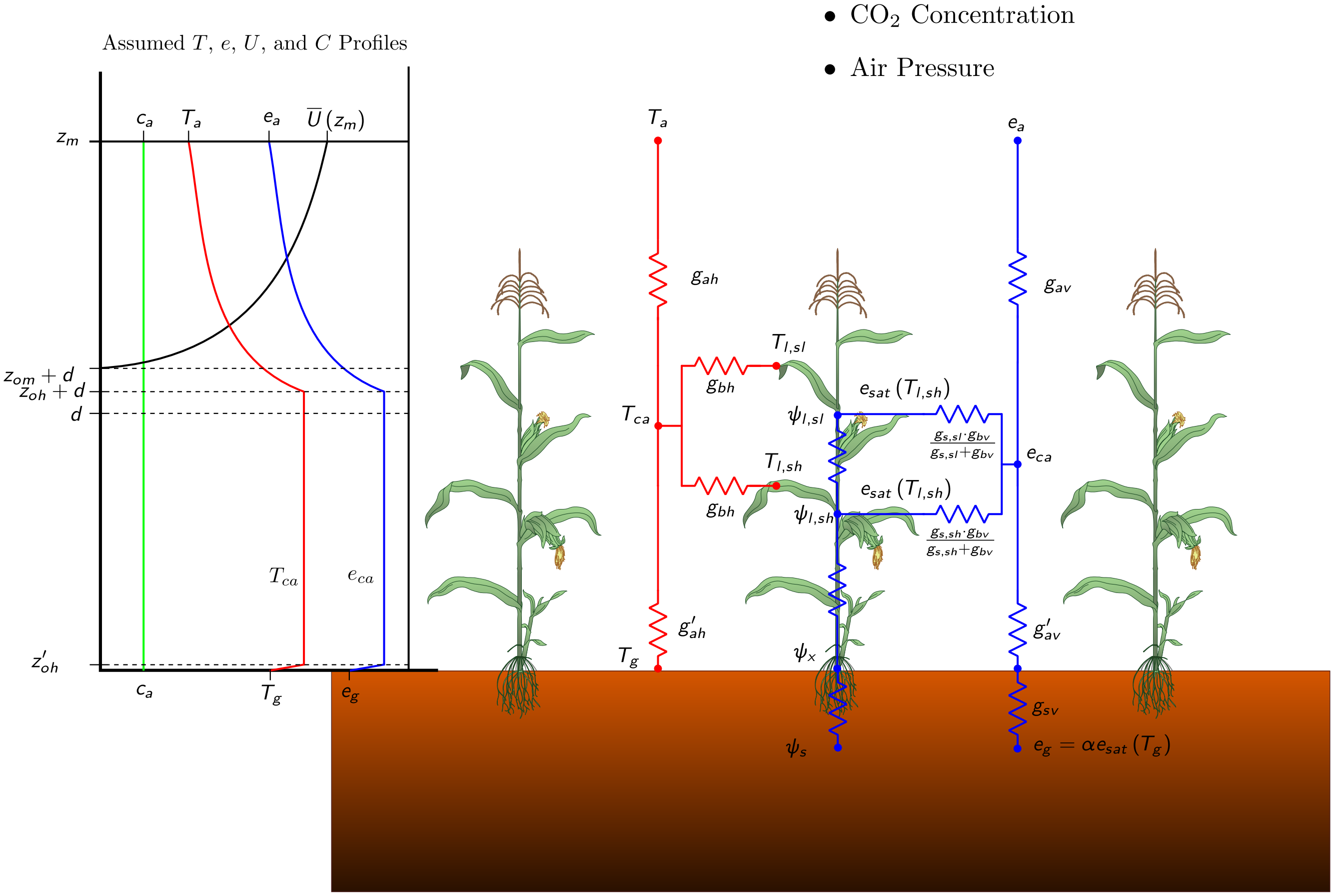

Figure S1. Schematic of our two-big-leaf, dual-source land surface model. The potentials and resistors indicate the scalar transport between the sunlit and shaded big leaf approximations, ground, canopy airspace and atmosphere. To the left are the assumed profiles of water vapor pressure deficit e, temperature (T), CO_2 partial pressure (c), and streamwise mean velocity ($\overline{U}$). The main modules used are laid out in text as well as the environmental forcings used from the US-Me2 AmeriFlux site for our simulations.

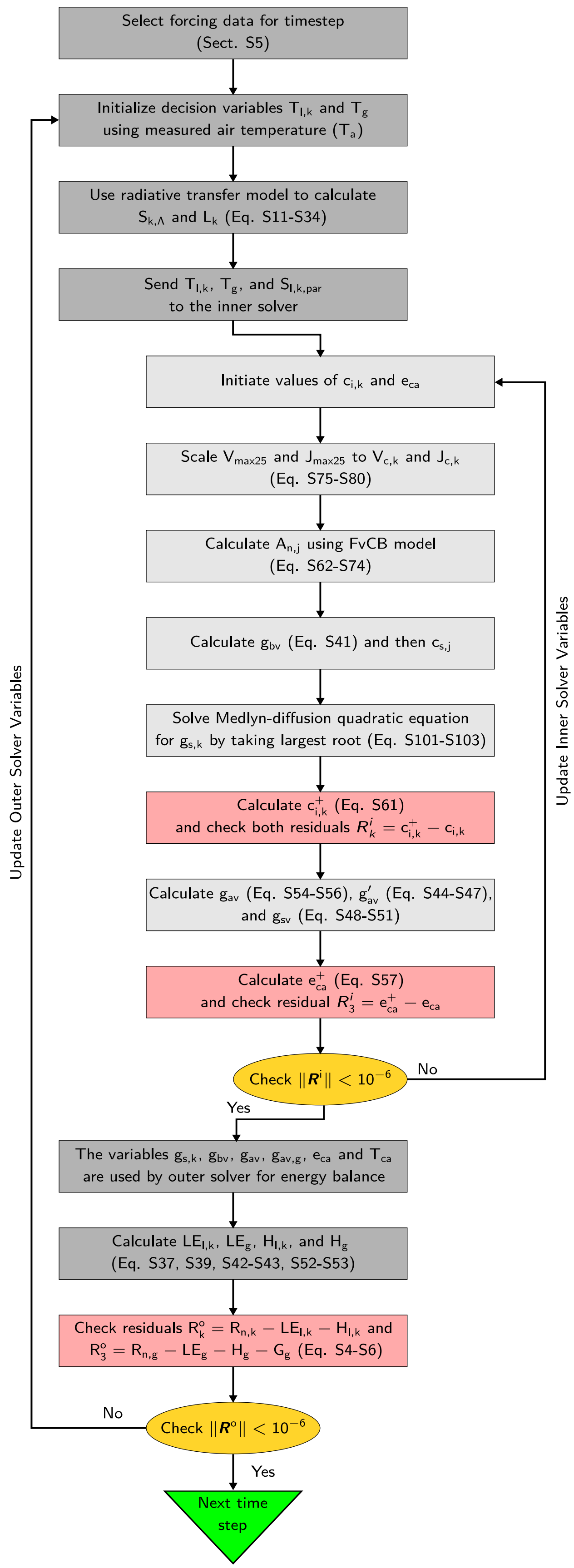

Figure S2. The well-watered solver solution scheme representing the outer solver (dark gray) and inner solver (light gray). Light red panels indicate a step where a residual to the nonlinear least squares problem is calculated and yellow indicates checking values of the residuals.

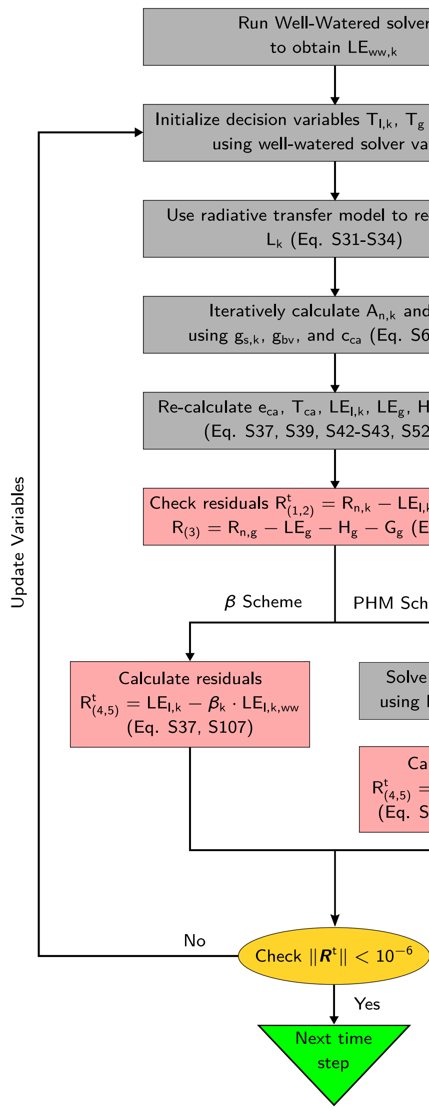

Figure S3. The transpiration downregulation scheme that is used after the well-watered solver to re-caclulate fluxes and states as plants reduce transpiration from soil water stress. Light red panels indicate a step where a residual to the nonlinear least squares problem is calculated and yellow indicates checking values of the residuals. There are two separate choices for downregulation: the β model and the Plant Hydraulic Model (PHM). See text for more details.

S3 LSM Variables, Parameters, and Forcings

The sheer volume of equations and data discussed in this supplemental materials make it necessary to provide a comprehensive table of variables, parameters, and constants with sources where necessary. This table has been split up based on the sections describing the LSM: radiative transfer (Table S1), scalar transport (Table S2), coupled stomatal conductance and photosynthesis (Table S3), transpiration downregulation (Table S4), and constants (Table S5). We break down each table, except for Table S5, into subscripts, fluxes and states, forcing data, and parameters. The 'subscripts' section is used to cut down on table entries as many subscripts are used on fluxes and parameters to describe their position in the the dual-source, two-big-leaf framework. The 'fluxes and states' section shows the main fluxes and states used in the section without all the positional subscripts. The 'forcing data' section highlights the US-Me2 site data used to force the model discussed in Sect. S5. The 'parameters' section contains all the functional and constant parameters used along with values and sources.

Table S1. The main fluxes, states and parameters used by the radiative transfer module of the LSM.

Name	Description	Value	Units	Sources
Subscript				
l	Plant canopy	-		
sl	Sunlit big leaf	-		
sh	Shaded big leaf	-		
k	Sunlit or shaded big leaf	-		
par	Photosynthetically active radiation (PAR)	-		
nir	Near infrared radiation (NIR)	-		
Λ	PAR or NIR	-		
b	Direct beam radiation	-		
d	Diffuse radiation	-		
sb	Scattered beam radiation	-		
in	Incoming radiation	-		
out	Outgoing radiation	-		
Fluxes and States				
S	Absorbed shortwave radiation	-	$W \cdot m^{-2}$	
L	Absorbed longwave radiation	-	$W \cdot m^{-2}$	
T	Temperature	-	^oC	
Forcing Data				[31,32]
S_{in}	Incoming shortwave radiation	-	$W \cdot m^{-2}$	
$S_{in,par}$	Incoming PAR	-	$W \cdot m^{-2}$	
$S_{in,par,d}$	Diffuse incoming PAR	-	$W \cdot m^{-2}$	
L_{in}	Incoming longwave radiation	-	$W \cdot m^{-2}$	
T_a	Air temperature at measurement height	-	^oC	
Parameters				
K	Extinction coefficient	-	-	
K'	Extinction coefficient corrected for single-scattering	-	-	
$\alpha_{l,par}$	PAR leaf absorption coefficient	0.74	-	Calibrated
$\alpha_{l,nir}$	NIR leaf absorption coefficient	0.43	-	Calibrated
LAI	Leaf area index	3.2	m^2 leaf area$\cdot m^{-2}$ ground area	Calibrated
τ	Transmissivity	-	-	
$G(Z)$	Mean leaf angle	-	radians	
Z	Solar zenith angle	-	radians	
χ_l	Leaf angle distribution parameter	0.11	-	Calibrated
$\rho_{l,h}$	Leaf reflectance for infinite horizontal canopy	-	-	
ρ_l	Plant canopy reflectance for infinite canopy	-	-	
ρ_l'	Plant canopy reflectance accounting for ground reflectance	-	-	
$\rho_{g,par}$	PAR ground reflectance	0.1	-	[16]
$\rho_{g,nir}$	NIR ground reflectance	0.2	-	[16]
δ_l	Fraction of longwave radiation absorbed by canopy	-	-	
F_k	Fraction of sunlit or shaded leaf area index	-	-	

Table S2. The main fluxes, states and parameters used by the scalar transport module of the LSM.

Name	Description	Value	Units	Sources
Subscript				
l	Plant canopy	-		
sl	Sunlit big leaf	-		
sh	Shaded big leaf	-		
k	Sunlit or shaded big leaf	-		
i	Inside the stomatal cavity of the leaf	-		
s	On the leaf surface	-		
g	Ground/soil	-		
ca	Canopy airspace	-		
a	Atmosphere above canopy at measurement height	-		
Fluxes and States				
LE	Latent heat flux	-	$W \cdot m^{-2}$	
H	Sensible heat flux	-	$W \cdot m^{-2}$	
e	Water vapor pressure	-	Pa	
T	Temperature	-	^oC	
c	CO_2 partial pressure	-	Pa	
Forcing Data				[31,32]
$\overline{u}$	Mean streamwise velocity	-	$m \cdot s^{-1}$	
u^*	Friction velocity	-	$m \cdot s^{-1}$	
θ_s	Soil water content at 50 cm depth	-	m^3 water$\cdot m^{-3}$ soil	
e_a	Water vapor pressure at measurement height	-	Pa	
T_a	Water vapor pressure at measurement height	-	^oC	
G	Ground heat flux	-	$W \cdot m^{-2}$	
Parameters				
g_s	Stomatal conductance	-	mol air $\cdot m^{-2} \cdot s^{-1}$ or $m \cdot s^{-1}$	
g_{bv} or g_{bh}	Leaf laminar boundary layer water vapor/heat conductance	-	$m \cdot s^{-1}$	
g_{av} or g_{ah}	Atmospheric water vapor/heat conductance	-	$m \cdot s^{-1}$	
g_{sv}	Soil pore to soil surface water vapor conductance	-	$m \cdot s^{-1}$	
g'_{av} or g'_{ah}	Soil to canopy airspace water vapor/heat conductance	-	$m \cdot s^{-1}$	
LAI	Leaf area index	3.2	m^2 leaf area$\cdot m^{-2}$ ground area	Calibrated
SAI	Stem area index	0.5	m^2 stem area$\cdot m^{-2}$ ground area	[33]
C_l	Leaf turbulent transfer coefficient	0.01	$m \cdot s^{-1}$	[2]
d_l	Characteristic leaf dimension	0.04	m	[2]
C_g	Ground turbulent transfer coefficient	-	$m \cdot s^{-1}$	
$C_{g,bare}$	Bare ground turbulent transfer coefficient	-	$m \cdot s^{-1}$	
$C_{g,dense}$	Dense canopy ground turbulent transfer coefficient	0.004	$m \cdot s^{-1}$	[2]
z_{om}	Atmospheric momentum roughness length	1	m	[11]
d_o	Zero-plane displacement	-	m	
z_{ov} or z_{ov}	Atmospheric water vapor/heat roughness length	0.1	m	[11]
$z_{om,g}$	Ground momentum roughness length	0.01	m	[2]
D_v	Water vapor diffusivity	-	$m^2 \cdot s^{-1}$	
DSL	Depth of dry soil layer	-	m	
D_{max}	Maximum dry layer thickness	0.015	m	
θ_{sat}	Saturated soil water content (porosity)	0.57	m^3 water$\cdot m^{-3}$ soil	[34]
θ_i	Soil water content where g_{sv} begins	0.57	m^3 water$\cdot m^{-3}$ soil	Calibrated
θ_{air}	Volumetric air content in soil pores	-	m^3 air$\cdot m^{-3}$ soil	
ϕ_{air}	Air filled pore space	-	m^3 air$\cdot m^{-3}$ pores	
τ	Soil pore tortuosity	-	-	
b	Brooks-Corey soil retention curve exponent	3.86	-	Calibrated
z	Measurement height	32	m	[31,32]
h_v	Vegetation height	18	m	[31,32]

Table S3. The main fluxes, states and parameters used by the coupled stomatal conductance-photosynthesis module of the LSM.

Name	Description	Value	Units	Sources
Subscript				
l	Plant canopy	-		
sl	Sunlit big leaf	-		
sh	Shaded big leaf	-		
k	Sunlit or shaded big leaf	-		
i	Inside the stomatal cavity of the leaf	-		
s	On the leaf surface	-		
g	Ground/soil	-		
ca	Canopy airspace	-		
Fluxes and States				
A_n^d	Net CO_2 assimilation rate from diffusion	-	μmol $CO_2 \cdot m^{-2} \cdot s^{-1}$	
A_n	Net CO_2 assimilation rate from photosynthesis	-	μmol $CO_2 \cdot m^{-2} \cdot s^{-1}$	
A_c	Rubisco-limited CO_2 assimilation rate	-	μmol $CO_2 \cdot m^{-2} \cdot s^{-1}$	
A_j	Light-limited CO_2 assimilation rate	-	μmol $CO_2 \cdot m^{-2} \cdot s^{-1}$	
A_p	Product-limited CO_2 assimilation rate	-	μmol $CO_2 \cdot m^{-2} \cdot s^{-1}$	
A	CO_2 assimilation rate	-	μmol $CO_2 \cdot m^{-2} \cdot s^{-1}$	
c	CO_2 partial pressure		Pa	
Forcing Data				[31,32]
P_{atm}	Atmospheric Pressure	-	Pa	
Parameters				
g_s	Stomatal conductance	-	mol air $\cdot m^{-2} \cdot s^{-1}$ or $m \cdot s^{-1}$	
g_1	Medlyn slope parameter	0.88	$kPa^{0.5}$	Calibrated
g_o	Minimal stomatal conductance	10e-4	mol air $\cdot m^{-2} \cdot s^{-1}$ or $m \cdot s^{-1}$	[2]
g_{bv}	Leaf laminar boundary layer water vapor	-	$m \cdot s^{-1}$	
V_{max25}	Max Rubisco assimilation rate at 25^oC	122	μmol $CO_2 \cdot m^{-2} \cdot s^{-1}$	Calibrated
J_{max25}	Max electron transport rate at 25^oC	256	μmol $e^- \cdot m^{-2} \cdot s^{-1}$	$2.1 \cdot V_{max25}$
Γ	CO_2 compensation point	-	Pa	
o_i	O_2 partial pressure	-	Pa	
K_c	Rubisco Michaelis-Menten rate constant for carboxylation	-	Pa	
K_o	Rubisco Michaelis-Menten rate constant for oxidation	-	Pa	
K_n	Nitrogen extinction coefficient	0.7	-	[2]
I_{PSII}	Electron transport rate from photosystem II	-	μmol $e^- \cdot m^{-2} \cdot s^{-1}$	
Φ_{PSII}	Quantum efficiency of photosystem II	0.7	μmol $e^- \cdot$ (μmol photons$)^{-1}$	[2]
Θ_{PSII}	Curvature factor J_{max25} and I_{PSII} co-limitation	0.85	-	[2]
Θ_{cj}	Curvature factor A_c and A_j co-limitation	0.98	-	[2]
A_i	CO_2 assimilation rate co-limited by A_c and A_j	-	μmol $CO_2 \cdot m^{-2} \cdot s^{-1}$	
Θ_{ip}	Curvature factor A_i and A_p co-limitation	0.95	-	[2]
R_d	Dark respiration rate		μmol $CO_2 \cdot m^{-2} \cdot s^{-1}$	

Table S4. The main fluxes, states and parameters used by the transpiration downregulation module of the LSM.

Name	Description	Value	Units	Sources
<u>Subscript</u>				
l	Plant canopy	-		
sl	Sunlit big leaf	-		
sh	Shaded big leaf	-		
k	Sunlit or shaded big leaf	-		
i	Inside the stomatal cavity of the leaf	-		
s	On the leaf surface	-		
g	Ground/soil	-		
ca	Canopy airspace	-		
sx	Soil-to-xylem	-		
xl	Xylem-to-leaf	-		
la	Leaf-to-atmosphere	-		
ww	Well-watered rate	-		
max	Maximum value	-		
<u>Fluxes and States</u>				
LE	Latent heat flux	-	mol $CO_2 \cdot m^{-2} \cdot s^{-1}$	
ψ	Water potential	-	MPa	
e	Water vapor pressure	-	Pa	
<u>Forcing Data</u>				[31,32]
θ_s	Soil water content at 50 cm depth	-	m^3 water$\cdot m^{-3}$ soil	
<u>Parameters</u>				
g_s	Stomatal conductance	-	mol air $\cdot m^{-2} \cdot s^{-1}$ or $m \cdot s^{-1}$	
g	Segment-specific conductance	-	$m \cdot s^{-1} \cdot MPa^{-1}$	
$\psi_{s,sat}$	Saturated soil water potential	-5.5e-3	MPa	Calibrated
b	Brooks-Corey soil retention curve exponent	3.86	-	Calibrated
c	Brooks-Corey hydraulic conductivity exponent	-	-	
d	Adjusting factor for roots in soil conductance	0	-	Calibrated
$K_{s,sat}$	Saturated soil hydraulic conductivity	0.81	$m \cdot d^{-1}$	Calibrated
RAI	Root area index	11	m^2 root area$\cdot m^{-2}$ ground area	[35]
d_r	Fine root diameter	5e-4	m	[35]
Z_r	Effective rooting depth	1.1	m	[34]
$\psi_{x,50}$	Xylem water potential at 50% loss of conductance	-2.6	MPa	Fixed[36]
a	Xylem vulnerability curve shape parameter	0.54	-	Calibrated
K_{sap}	Sapwood-specific hydraulic conductivity	1.33	$kg \cdot m^{-1} \cdot s^{-1} \cdot MPa^{-1}$	Calibrated
$SapAI$	Sapwood Area Index	20e-4	m^2 sapwood $\cdot m^{-2}$ ground area	[37]
h_v	Vegetation height	18	m	[31,32]
$\psi_{l,50}$	Leaf water potential at 50% loss of stomatal conductance	-1	MPa	Fixed[38]
b_l	Leaf vulnerability curve shape parameter	5	-	Calibrated
LAI	Leaf area index	3.2	m^2 leaf area$\cdot m^{-2}$ ground area	Calibrated
Φ	Flux potential from Kirchhoff transform	-	$kg \cdot s^{-1}$	

Table S5. The main physical constants used in the LSM.

Name	Description	Value	Units
ρ_w	Density of water	1000	$kg \cdot m^{-3}$
ρ_a	Density of air	1.2	$kg \cdot m^{-3}$
ε	Molar ratio of water to air	0.622	-
$\mathscr{L}_v$	Latent heat of vaporization	2.5e6	$J \cdot kg^{-1}$
k	von Karmen constant	0.4	-
ν	Kinematic viscosity	1.5e-5	$m^2 \cdot s^{-1}$
R_g	Universal gas constant	8314	$J \cdot K^{-1} \cdot mol^{-1}$
c_p	Specific heat of air at constant pressure	1004	$J \cdot kg^{-1} \cdot K^{-1}$

S4 LSM Calibration

The LSM was calibrated using two-step approach consisting of a grid search followed by a parameter adjustment to ensure realistic values compared to measurements. The grid search created 13,600 parameter sets of 15 soil, plant and radiative parameters (Table S6) using Progressive Latin Hypercube Sampling available in the VARSTOOL package[39] in MATLAB. The 13,600 simulations were run for May-August 2013-2014 for the hours of 8 AM to 8 PM, excluding 12 hours following any precipitation event. The best parameter set from the grid search was then altered to align with plant hydraulic values from literature, while maintaining the same transpiration downregulation behavior. For clarity, we will refer to the best parameter set from the grid search analysis as 'Best' and the final adjusted parameter set used for the paper as 'Best*'.

We evaluated the grid search parameter sets based on a performance metric of evapotranspiration (ET), sensible heat flux (H), gross primary productivity (GPP) and net radiation (R_n) predictions. The performance metric (M_{cal}; Eq. S108) consists of Taylor diagram statistics[40]: 1) the correlation coefficient (R), 2) the centered root mean square error ($CRMSE$), and 3) the difference in simulation versus observed variance ($\Delta\sigma$). The percent bias (P_b) was also added to the metric to account for the mean difference in simulation and observation. Each index i in the summation of Eq. S108 represents a different flux which are combined to form a single metric.

$$M_{cal} = \sum_{i}^{n} \frac{R_i}{max(R)} - CRMSE_i - P_{b,i} - \frac{\Delta\sigma_i}{max(\Delta\sigma)} \tag{S108}$$

We selected the three VARSTOOL parameter sets (VT1-VT3) with the highest metric value and selected VT1 because it fit ET the best (Fig. S5-S7). From here, we adjusted VT1 by reducing $g_{xl,max}$ by 60% to reduce biases found in representing ET during water stressed conditions (Fig. S7). As mentioned in the article, this parameter set (labeled 'Best' in Table S6 and figures) had an unrealistically low $\psi_{l,50}$ value compared to measurements of ponderosa pine at other sites[38]. Therefore, we undertook the second step of our calibration method: altering calibrated plant hydraulic traits to align with literature values, while maintaining the transpiration downregulation behavior.

Our LSM suffers from equifinality[41] (i.e., multiple parameter sets yield similar predictions) due to epistemic errors and non-linearity in the model structure. Although equifinality is usually an undesirable modeling reality, we were able to leverage it to find a new parameter set ('Best*') with more realistic plant hydraulic trait values while matching the transpiration downregulation behavior of the original calibrated parameter set ('Best'). To do this, we ran our PHM (outside of the LSM) with the 'Best' parameter set to create relative transpiration curves (T^{phm}/T_{ww}; solid lines in S4) for the range of soil water content (θ_s from measurements) and well-watered transpiration (T_{ww} from the well-watered LSM simulation) experienced at the US-Me2 site. We specified θ_s rather than ψ_s because the soil water characteristic parameters (b, $\psi_{s,sat}$, and d) must be adjusted to alter the range of plant water potential experienced and, hence, the appropriate values of $\psi_{l,50}$ and $\psi_{x,50}$. We fixed $\psi_{l,50}$[38] and $\psi_{x,50}$[36] to desired literature values in our PHM and tuned the remaining six hydraulic parameters within realistic ranges (K_{sap}, a, b_l, b, $\psi_{s,sat}$, and $K_{s,sat}$) until the new relative transpiration curves (dots in Fig. S4) matched the 'Best' curves. We used nonlinear least squares to perform the tuning with the residual being the difference between the original and new relative transpiration curves. The resulting tuned parameters, which we call 'Best*' (Table S6), match the transpiration downregulation behavior of our original calibration almost perfectly (Fig. S4). It is worth noting that the correction factor d in Brooks-Corey needed to be set to zero (from its original value of 4[27]) in this second step in order to obtain realistic values for the soil water exponent, b. Overall, this two-step approach successfully creates a parameter set consistent with literature values and capable of matching observations.

The metric value for all parameter sets used in our calibration are shown in Fig. S5 in terms of R and $CRMSE$. Specifically, we highlight the three top sets from the VARSTOOL grid search simulations (VT1-VT3) as well as the 'Best' and 'Best*'that show the clear trade-off in improvements between ET, H, GPP, and R_n. The outgoing longwave (L_{out}) and shortwave radiation (S_{out}) were ignored as including them in the metric had minimal effect on the selected parameter sets. The 'Best*' (red x) and 'Best' (pink diamond) provide clear improvement to the R and $CRMSE$ compared to VT1-VT3 for ET. Similarly, the median diurnal fluxes for the observations and five selected LSM runs during May-June (Fig. S6) and July-August (Fig. S7) reveal the largest performance differences between parameter sets are for ET and GPP predictions. The over-prediction of ET by VT1-VT3 during soil water stress (Fig. S7) informed our decision to create the 'Best' (and 'Best*') parameter set by reducing $g_{xl,max}$ to correct the bias. This manual adjustment also provides slight performance increases to some second order statistics of the fluxes illustrated in the Taylor diagram[40] in Fig. S8. The adjustment from 'Best' to 'Best*' has minimal impact when looking at Fig. S5-S8; most notably, the diurnal ET and GPP for late summer (Fig. S7) are slightly different. However, this difference has no effect on the main conclusions on the differences between PHMs and β based on the LSM analysis of the US-Me2 site.

The 'Best*' parameters set fit the ET observations well, but, as illustrated in Fig. 5e of the article, the β_s downregulation scheme does perform best for a few T_{ww}-θ_s. Looking at the P_b statistic for β_s, PHM and well-watered LSM runs (Fig. S9), we see β_s has the best performance for particular bins (bins outlined in red) where the PHM over-regulates because the β_s is fit to the mean PHM behavior and downregulates less. However, in bins with higher (lower) T_{ww} than the selected bins, β_s underregulates (overregulates) as expected. More generally, any performance improvement from β_s would be due to inadequate model fit for the PHM and not β_s capturing the physics. Because β_s is an end member scenario of a PHM, the best possibility for β_s is that it predicts the same as the PHM, which means the complexity of a PHM is unnecessary to represent a certain soil-plant system. Therefore, in terms of Fig. 5e, β_s is right for the wrong reasons as it outperforms the PHM for a small region where the underlying PHM parameter fit is likely not optimal and could be corrected by further calibration.

Table S6. The calibration parameters for the LSM with PHM downregulation scheme. The parameter ranges were used to create 13,600 parameters sets that were each run in the LSM. The initial calibrated value was selected based a performance metric (Eq. S108) and additional manual adjustment ('Best'), while the final calibrated values used in the article ('Best*') were created by replicating the transpiration downregulation behavior of the 'Best' parameter set with $\psi_{l,50}$ and $\psi_{x,50}$ set to literature values.

Parameter	Description	Range	Units	**Calibrated Values** Best	Best*
K_{sap}	Sapwood-specific hydraulic conductivity	[5e-4,5e1]	kg m^{-1} s^{-1} MPa^{-1}	0.28	1.33
$\psi_{x,50}$	Xylem water potential at 50% loss of xylem conductance	[-0.1,-15]	MPa	-2.3	-2.6
a	Xylem vulnerability curve shape parameter	[0.2,10]	-	0.3	0.54
$\psi_{l,50}$	Leaf water potential at 50% loss of stomatal conductance	[-0.1,-15]	MPa	-9.9	-1
b_l	Leaf vulnerability curve shape parameter	[0.2,5]	-	3.4	5
b	Soil retention curve exponent	[2,14]	-	5.1	3.86
$\psi_{s,sat}$	Saturated soil water potential	[1e-3,1e-2]	MPa	9.9e-3	5.5e-3
$K_{s,sat}$	Saturated soil hydraulic conductivity	[0.01,20]	m d^{-1}	10	0.81
θ_i	Incipient soil water content for restricting bare soil evaporation	[0,0.57]	-	0.57	Same
g_1	Medlyn Slope Parameter	[0.5,5]	kPa$^{0.5}$	0.9	Same
$V_{max,25}$	Max Rubisco-limited carboxylation rate	[5,200]	μmol CO_2 m^{-2} s^{-1}	122	Same
LAI	Leaf area index	[1.5,4]	m^{-2} LA m^{-2} GA	3.2	Same
$\alpha_{l,par}$	Leaf reflectance to PAR	[0.5,1]	-	0.74	Same
$\alpha_{l,nir}$	Leaf reflectance to NIR	[0,0.6]	-	0.43	Same
χ_l	Leaf angle distribution parameter	[-0.4,0.6]	-	0.11	Same

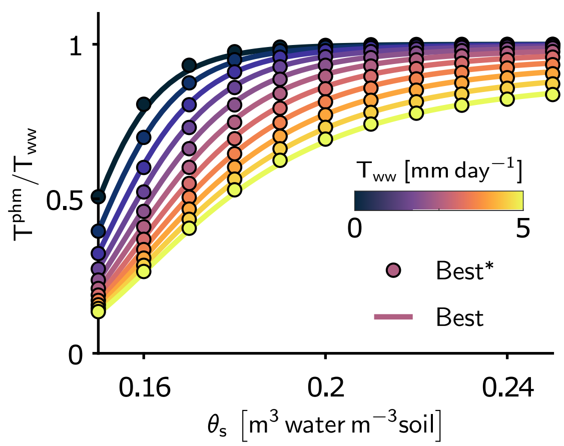

Figure S4. The matching of downregulation behavior for the initial (Best; solid lines) and final (Best*, dots calibration parameter values shown in Table S6. We had to adjust our Best model parameters given a few unrealistic values compared to measurements (see text for more details). Matching the relative transpiration outputs (T^{phm}/T_{ww}) over the range of soil water content (θ_s) measurements used to force the model yielded nearly identical flux predictions between Best and Best* parameter sets.

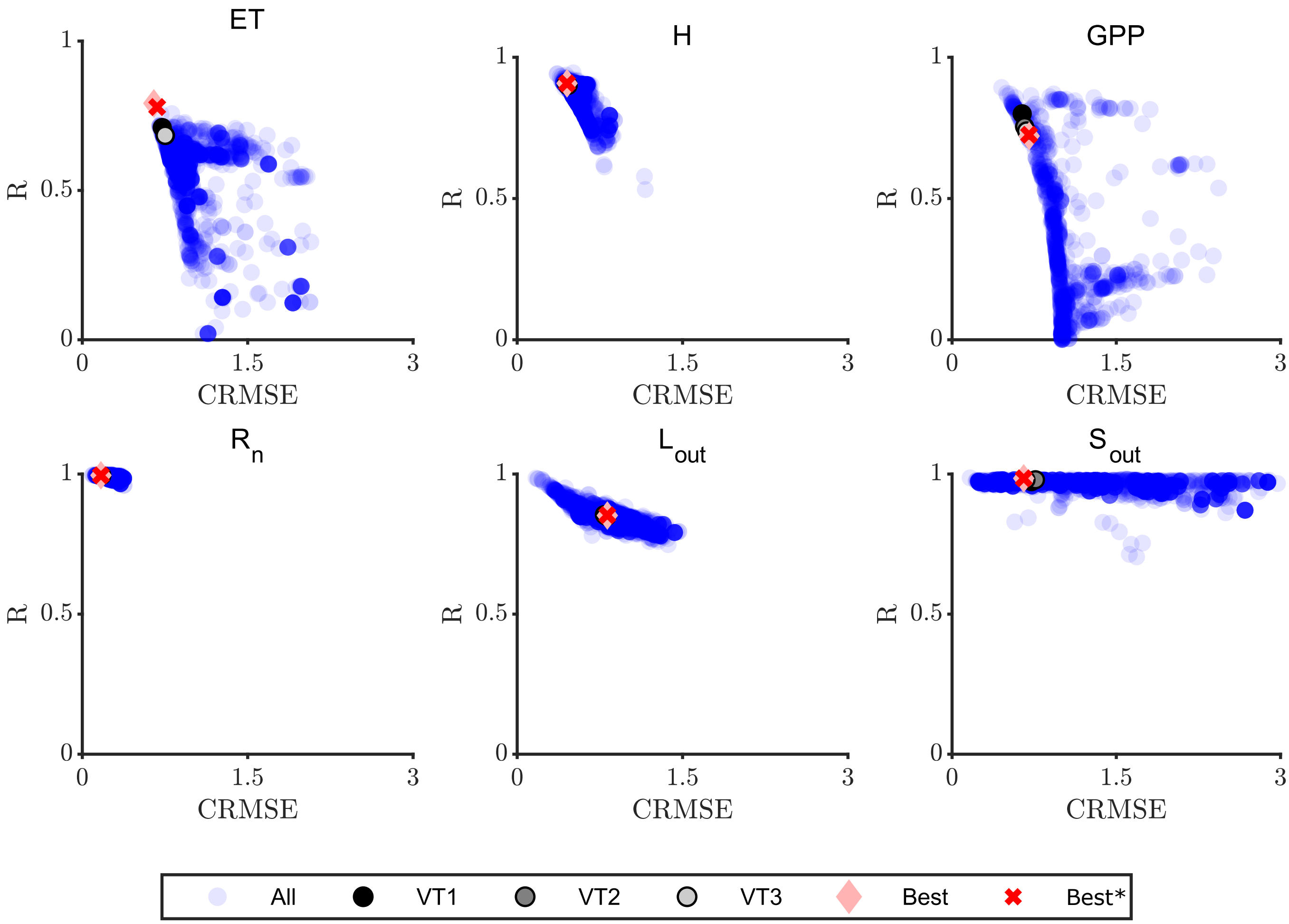

Figure S5. Centered root mean square error (CRMSE) and correlation (R) statistics for the LSM with PHM downregulation scheme for 13,600 parameters sets plus two adjusted parameter sets. An ideal score would be R = 1 and CRMSE = 0. The best fits from the VARSTOOL-created parameters sets, labelled VT1-VT3, are based on the metric in Eq. S108, while a manual adjustment to VT1 was used to create the 'Best' and 'Best*' parameter sets. The 'Best*' parameter set is used in the main article for our calibrated LSM with PHM downregulation scheme.

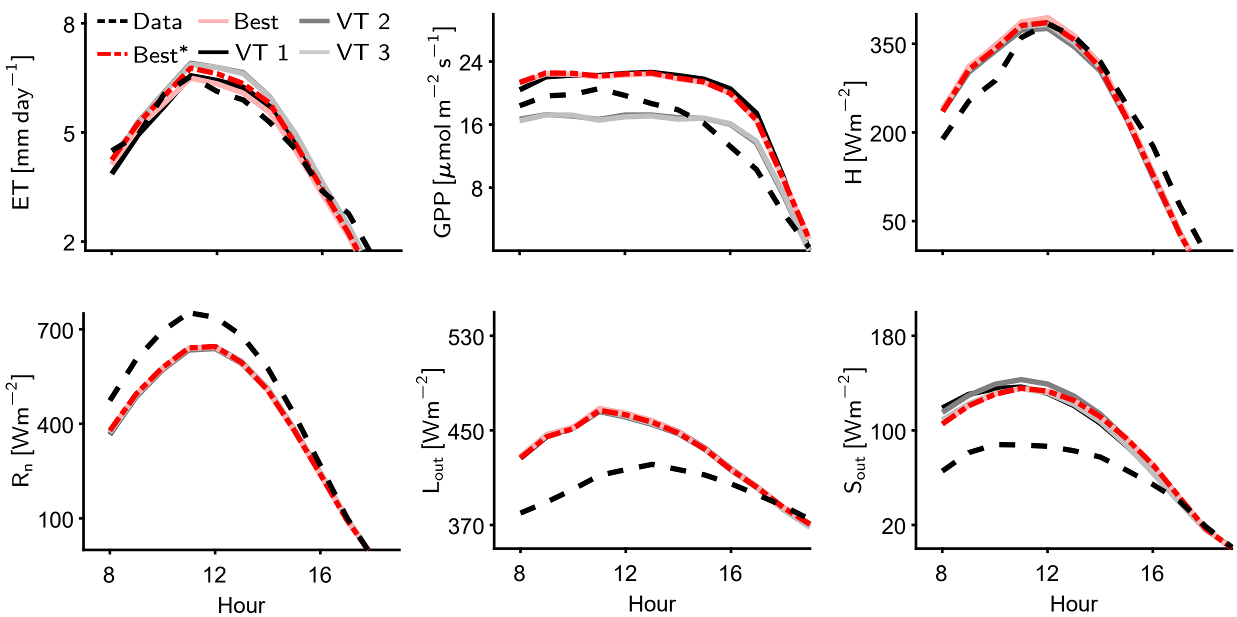

Figure S6. The median diurnal fluxes for May-June 2013-2014 for the three best VARSTOOL parameter sets (VT1-VT3) and the initial ('Best') and final ('Best*') calibrated parameter set compared to the US-Me2 flux data for evapotranspiration (ET), gross primary productivity (GPP), sensible heat flux (H), net radiation (R_n), outgoing longwave radiation (L_{out}) and outgoing shortwave radiation (S_{out}).

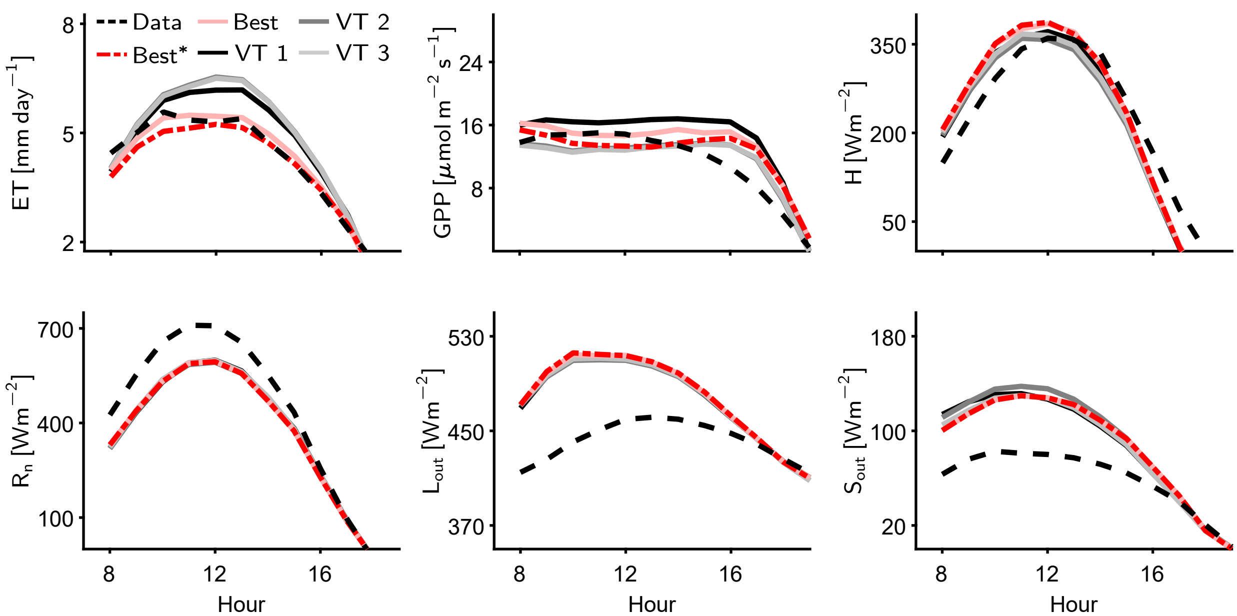

Figure S7. Same as Fig. S6 for July-August 2013-2014 where there is soil water stress.

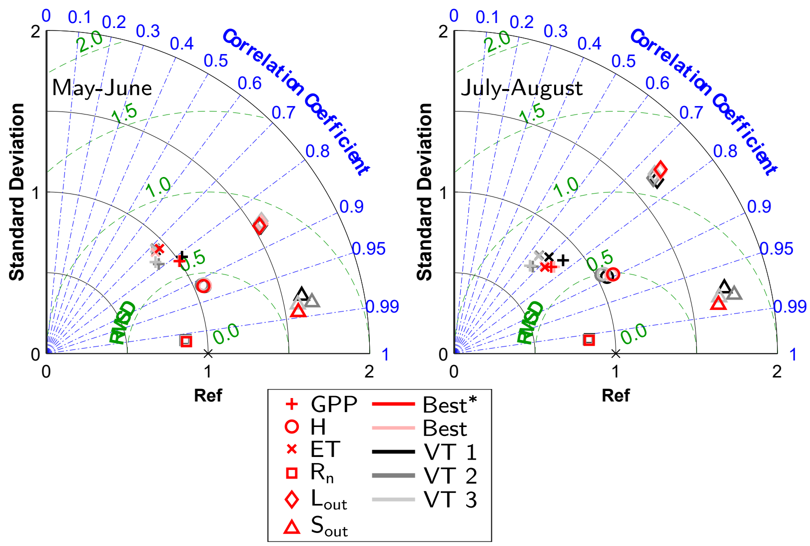

Figure S8. The Taylor diagrams for May-June 2013-2014 (left) and July-August 2013-2014 (right) for the three best VARSTOOL parameter sets (VT1-VT3) and the initial ('Best') and final ('Best*') calibrated parameter set compared to the US-Me2 flux data for Evapotranspiration (ET), gross primary productivity (GPP), sensible heat flux (H), net radiation (R_n), outgoing longwave radiation (L_{out}) and outgoing shortwave radiation (S_{out}).

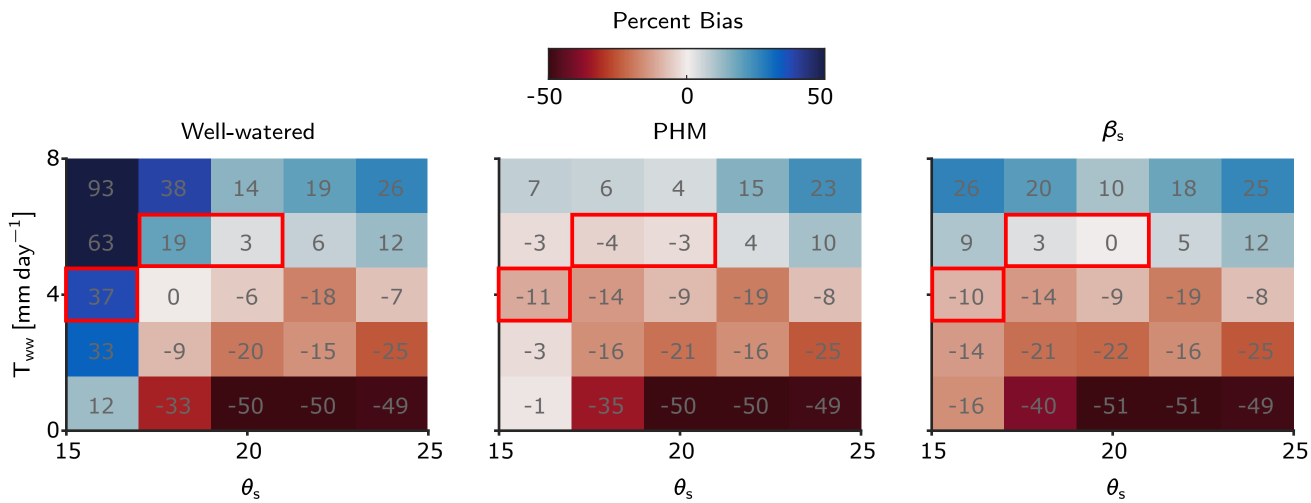

Figure S9. The percent bias (P_b) of the LSM with well-watered, PHM and β_s downregulation schemes compared to ET observations at the US-Me2 flux tower site. The P_b is broken down by well-watered transpiration T_{ww} and volumetric soil water content (θ_s) as in Fig. 5e-f of the main article. The gray numbers give the exact P_b value for each bin while the red outline highlights the primary bins where β_s appears to outperform the PHM in Fig. 5e of the main article. See text for explanation.

S5 LSM Forcing Data

The LSM for the AmeriFlux US-Me2 ponderosa pine site was forced with half-hourly atmospheric and subsurface measurements at the site taken from both the FLUXNET2015[31,42] and AmeriFlux datasets[32]. Primarily, we used the FLUXNET2015 dataset, which performs additional gap-filling and quality control on the AmeriFlux dataset using a standard processing pipeline. However, we obtained the soil moisture and temperature profiles from the AmeriFlux dataset as only a single depth was included in the FLUXNET2015 dataset. For simplicity, we use the label 'AmeriFlux US-Me2' to refer to this site and dataset. This site was specifically selected for the LSM case study based on its extensive subsurface soil moisture and temperature profiles as well as its separate measurements of photosynthetically active radiation (PAR) and near infrared radiation (NIR). The extensive soil moisture and temperature data and detailed shortwave radiation measurements were used as forcing for the LSM in lieu of one-dimensional mass and heat transfer equations and atmospheric radiation partitioning models. The main focus of this work was on the scalar transport of the LSM, so use of these measurements help reduce confounding errors from other model structures (although there would still be measurement errors).

The following atmospheric measurements from the AmeriFlux US-Me2 site for May-August 2013-2014 were used to force the LSM: friction velocity (u^*), mean streamwise velocity ($\overline{u}$), air temperature (T_a), water vapor pressure (e_a), atmospheric pressure (P_{atm}), and CO_2 partial pressure (c_a). The radiative site measurements consisted of total incoming shortwave (S_{in}) and longwave radiation (L_{in}) as well as total and diffuse PAR. The LSM requires partitioning of shortwave radiation into PAR and NIR as well as direct beam and diffuse quantities. The diffuse incoming PAR ($S_{in,par,d}$) was measured at the site and the direct beam PAR ($S_{in,par,b}$) was calculated by the difference of total PAR ($S_{in,par}$) and diffuse PAR. Unfortunately, the site did not differentiate between direct beam ($S_{in,nir,b}$) and diffuse NIR ($S_{in,nir,d}$); therefore, total NIR was partitioned using the same ratio of direct and diffuse PAR at every time step. These detailed radiation measurements constrained the use of data from 2013-2014, as this was when they were most consistently available.

The subsurface moisture and temperature data was used to calculate the soil water availability of the root zone and the ground heat flux G at each time step. The G used to force the model was simply the thermopile measurements at 5 cm. In contrast, selecting a depth for the soil water content (θ_s) that would be representative of root-zone soil water availability was more difficult given there is minimal information at the US-Me2 site about the root structure. The US-Me2 site has θ_s measurements at 10, 20, 30, 50, 70, 100, 130, and 160 cm at multiple locations. To select a representative depth, we analyzed GPP deviations from the mean in terms of θ_s and vapor pressure deficit (D) at each depth (Fig. S10). All GPP values were studentized (i.e., mean subtracted and normalized by standard deviation) by hourly subsets for the period of May-August 2002-2014 to remove diurnal variation in flux magnitude and the median of these scores is plotted for each θ_s-D bin. The blue (red) values indicate lower (higher) than average GPP fluxes. As expected, measurements at each depth show lower values during water stress periods (low θ_s and high D). However, the ranges of θ_s experienced varies with depth, likely due to the combined effects of variable soil moisture profile, soil texture heterogeneity, and sensor inaccuracy. We selected the depth of 50 cm to use as our soil moisture forcing for two reasons: 1) there is a clear signal of GPP downregulation covering a wider range of soil moistures, and 2) a depth of 50 cm seems reasonable to represent the average moisture conditions when looking at meta-analyses of temperate coniferous forest root measurements[43].

A crucial consequence of using the subsurface inputs as model forcings is that it allowed the model time steps to be run in parallel. Typically, the model must be run sequentially since the subsurface models are partial differential equations in space (soil column) and time, and each time step relies on previous energy stored in the subsurface. The observations codify this temporal information, thereby allowing the LSM to run steady-state energy partitioning on top of the temporal dynamics of soil moisture and heat. Additionally, the LSM simulation was run only for time steps 24 hours after precipitation, since the model was not coded to handle canopy precipitation interception. Lastly, atmospheric stability effects were ignored for simplicity, as they add an additional layer of complexity to the solution scheme[5].

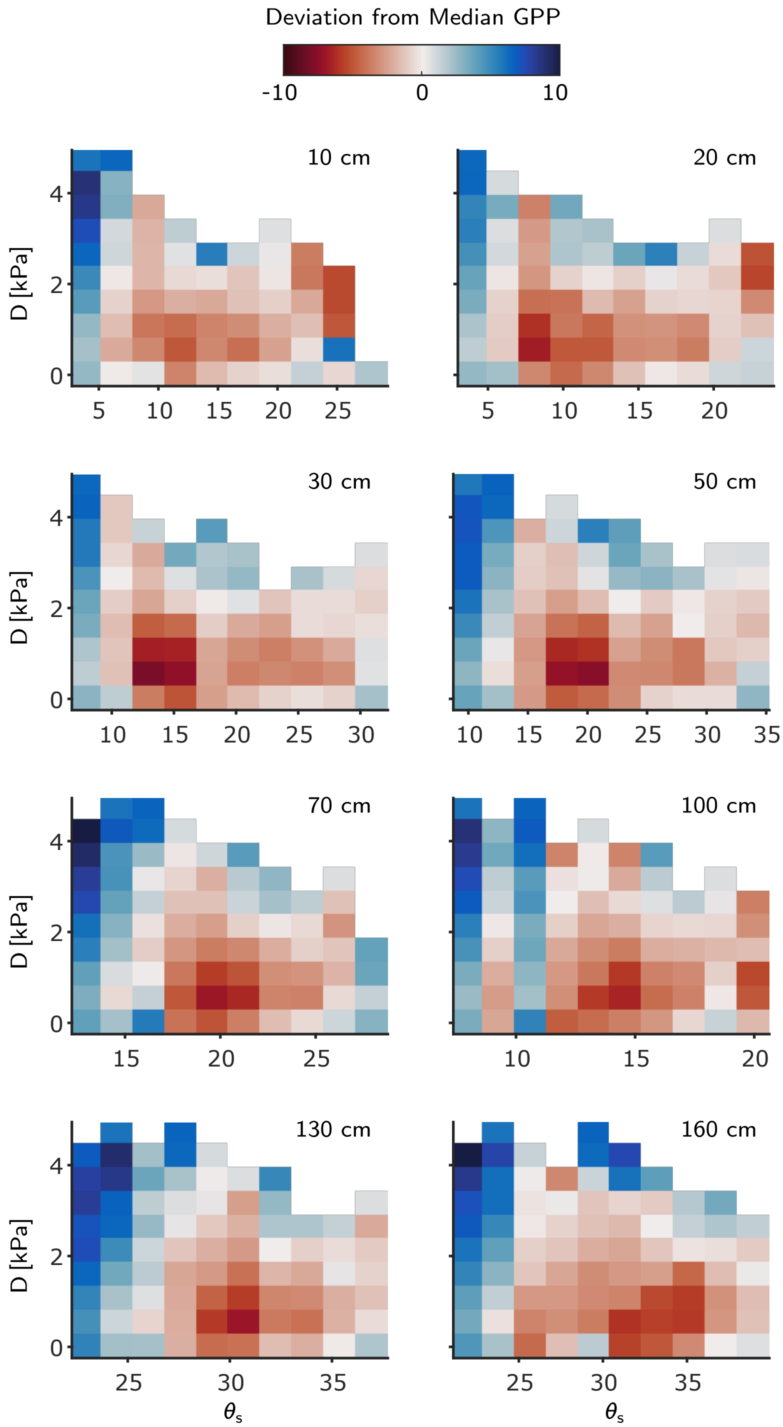

Figure S10. Median scores of the studentized gross primary productivity (GPP) measurements at the US-Me2 flux site for differing depth so soil water content θ_s measurements. The θ_s and vapor pressure deficit (D) measurements help identify water stress periods. The GPP data used are from May-August 2002-2014 and are studentized by their hourly subset to remove diurnal variations. Blue (red) in the plots is an indicator of decreased (increased) GPP from the mean value.

S6 Additional LSM Results

S6.1 Soil Water Availability and Atmospheric Moisture Demand

The improved performance of PHMs during midday of July-August (Figs. 5c-d in the article) are explained by looking at the temporal breakdown of the well-watered transpiration (T_{ww}) and site data of soil water availability (Fig. S11). The T_{ww} is a proxy for stomata-regulated atmospheric moisture demand at the site and is the greatest from 10 AM to 3 PM during the later summer months. The measured volumetric water content shows water stress during the later summer months as well. Therefore, these diurnal results suggest that PHMs are most important during periods of high atmospheric moisture demand and low soil water availability.

S6.2 Fitting β Schemes

The three β transpiration downregulation schemes used in this work were calibrated by fitting their respective parameters to the outputs of the calibrated LSM that uses a PHM scheme (the calibration process is detailed more extensively in Sect. S4). The calibrated LSM outputs are relative transpiration, T/T_{ww}, for the sunlit and shaded big leaf (dots in Fig. S12e-f). We decided to avoid calibrating each LSM directly with a β scheme to the site data, and instead derive the β scheme from a fitted PHM scheme, because we know β is an end-member scenario of a PHM. Therefore, this process allows us to check if the complexity of a PHM is necessary to represent transpiration downregulation without confounding factors of differently calibrated parameter sets.

The single β scheme (β_s) has a Weibull curve (Eq. 13 in the article) fit to the combined calibrated sunlit and shaded T/T_{ww} using nonlinear least squares in MATLAB. The fitted β_s parameter values for $\psi_{s,50}$ and b_s are -0.74 MPa and 3.3, respectively (shown in Fig. S12a-d in light gray). The two-leaf β scheme (β_{2L}) fits a β curve to the calibrated sunlit and shaded T/T_{ww} separately. The fitted β_{2L} parameter values for $\psi_{l,50}$ and b_l are -0.70 (-0.78) MPa and 2.7 (4.1) for the sunlit (shaded) big leaf (shown in Fig. S12a-d in dark gray). The reader is referred to Sect. S2.6.2 for details of how these β curves are used in LSM calculations.

The 'dynamic β' scheme (β_{dyn}) was fit to the calibrated T/T_{ww} using a two-step process. First, the T/T_{ww} values were parsed into 10 bins covering the T_{ww} range for the sunlit and shaded big leaf separately and a single β curve was fit to each bin (black circles in Fig. S12a-d). Second, a line was fit to the parameters $\psi_{s,50}$ and b_s as a function of T_{ww} (red lines and equations in Fig. S12a-d) using least squares weighted by T_{ww}. Therefore, the parameters of β can dynamically change with the atmospheric moisture demand represented by T_{ww}. This is illustrated in Fig. S12e-f by the β_{dyn} lines at fixed T_{ww} values that closely match the color gradation of the calibrated T/T_{ww} envelope. The variation of β_{dyn} with respect to T_{ww} is well described by linear parameter functions for the PHM we have fit to this US-Me2 site.

The β_{dyn} has great potential to parsimoniously represent the complexity of a PHM given the simplistic, linear parameter functions ($b_s(T_{ww})$ and $\psi_{s,50}(T_{ww})$). The intercepts of the parameter functions for sunlit and shaded leaves are very similar. Furthermore, although the slope of the shaded leaf parameter functions (Fig. S12b,d) are steeper than the slope of the sunlit parameter functions (Fig. S12a,c), the behavior is consistent when looking at the sunlit bin fits (circles in Fig. S12a,c) for the matching T_{ww} range of 0-3 mm/day. During lower atmospheric moisture demand, the linear parameter functions are steeper, but become more gradual at higher T_{ww}. Therefore, fitting $b_s(T_{ww})$ and $\psi_{s,50}(T_{ww})$ to combined sunlit and shaded points (i.e., not having different sunlit and shaded functions) should work well. Additionally, we could attempt to fit a parsimonious curvilinear function to the combined sunlit and shaded points (e.g., Weibull function) to reduce errors when fitting to low T_{ww}. Regardless, these results indicate that the complexity of our PHM can be represented by a 'dynamic β' with 4 total parameters (2 slope and 2 intercept), which is only two more parameters than the original β model. A promising avenue of future work is to relate these four parameters to key plant hydraulic traits and soil parameters to allow general application of the 'dynamic β' to sites other than US-Me2. Currently, modelers could attempt to use the linear parameter functions to parsimoniously calibrate an LSM with a 'dynamic β' scheme to site data; however, further work must validate these linear forms.

S6.3 RMSE Comparison of PHM and β Schemes

The improvements of the PHM scheme to the β_s and 'dynamic β' schemes are shown in terms of reduction in percent bias in Fig. 5e-f. These results are corroborated by the change in root mean square error as shown in Fig. S13. The RMSE results only differ from those based on reduction in percent bias in terms of improvements that are concentrated toward the highest T_{ww} periods, since that is where the highest magnitude errors occur.

S6.4 LSM Cumulative Energy and Carbon Budget Errors

To aid the interpretation of the LSM case study, we have also calculated the cumulative error for our five LSM schemes compared to key measured fluxes at the US-Me2 site (Table S7-S8) during periods of high ($T_{ww} \geq 4$ mm day^{-1}) and low ($T_{ww} < 4$ mm day^{-1}) atmospheric moisture demand. We split the table based on demand because β_s over-predicts ET under high demand and under-predicts ET during low demand, which results in misleadingly low cumulative errors. The β_s gets the right answer for the wrong reasons as errors from high demand periods are corrected by other errors from low demand periods. By splitting the table, we disentangle (at least somewhat) this error compensation. Furthermore, we did not split the table based on soil water stress as the effects of PHMs are seen at nearly all soil moisture values during high demand, and only at low soil moisture values during low demand (Fig. S13).

The PHM and β_{dyn} schemes provide the reduction in cumulative error ($\sim$5%) to evapotranspiration (ET) and gross primary productivity (GPP) during high atmospheric moisture demand, with less consistent results during low atmospheric moisture demand. Although these error reductions seem small and are likely outweighed by energy balance closure errors in the flux tower data (up to 20%[44]), they—along with the improvements in percent bias (Fig. 5e-f) and root mean square error (Fig. S13)—are consistent with our theoretical analysis of the fundamental differences between β and PHMs under varying environmental conditions. Therefore, we expect these errors to persist and grow under longer simulations and more variable environmental conditions.

The PHM scheme does not universally improve all energy and mass balance components. β_s appears to slightly improve sensible heat flux (H) in all conditions and GPP under low demand, while the differences in net radiation (R_{n}) and outgoing longwave radiative flux (L_{out}) appear insignificant for all models. A reason for less consistent results between PHM and β during low demand could be our calibration process uses a metric that focuses on fitting larger fluxes which happen during higher atmospheric moisture demand. Furthermore, from all of our analysis, we know β_s is not improving predictions because it is capturing a physical process better than PHMs. We know β_s is the end-member scenario of a PHM, so β_s can only perform the same or worse than a PHM and give us the answer to, "Is the complexity of a PHM necessary?". Any improvements from β_s represent confounding errors in our parameter fit, observations and model structure.

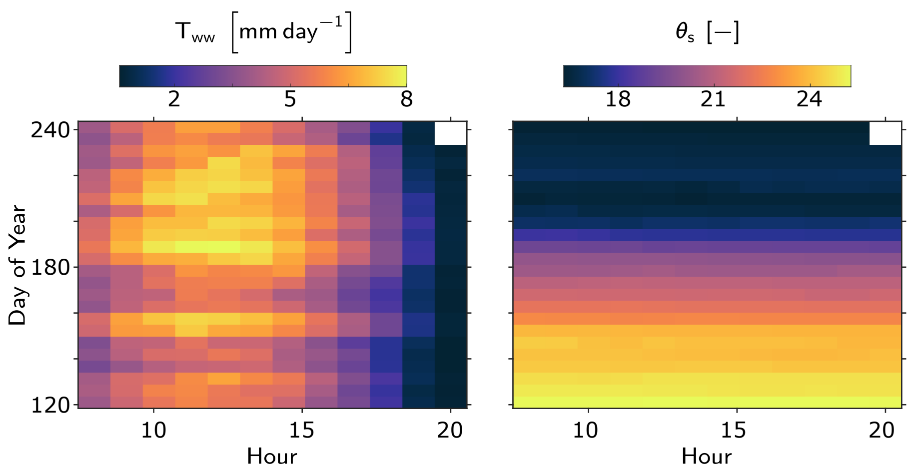

Figure S11. Left: Well-watered transpiration rate calculated form the LSM run with no transpiration downregulation. This is a proxy for the stomata-regulated atmospheric moisture demand. Right: Measured volumetric water content of soil at the US-Me2 site at 50 cm depth. The colors are the average value for the temporal bins for May-August 2013-2014.

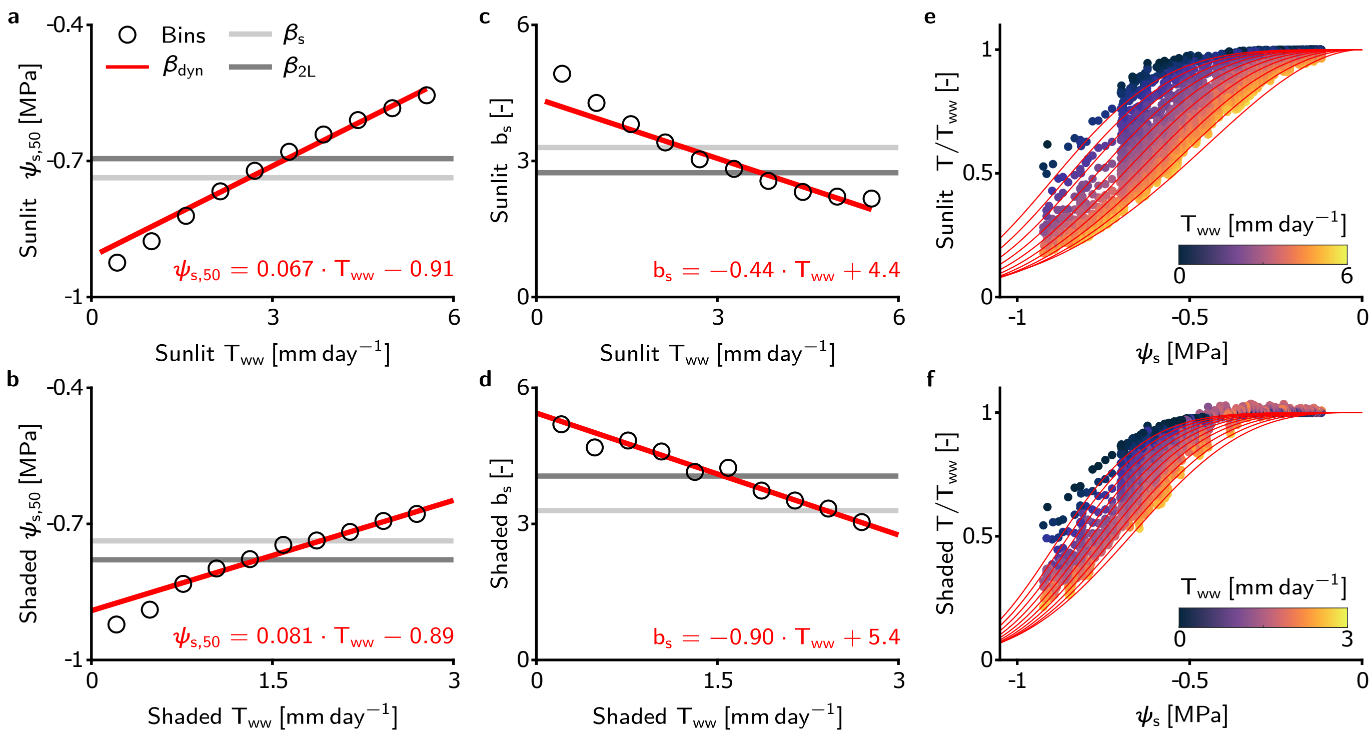

Figure S12. The 'dynamic β' (β_{dyn}) fits used for the sunlit (top row) and shaded big leaf (bottom row). The first column is the dependence of the soil water potential at 50% loss of stomatal conductance on well-watered transpiration T_{ww}. The second column is the dependence of the stomatal sensitivity parameter (b_s) to T_{ww}. The black circles are parameter values fit to relative transpiration (T/T_{ww}) binned over the range of T_{ww}. The linear relationship for both parameters is shown in red. The last column shows the relative transpiration outputs from the calibrated PHM with dot colors corresponding to T_{ww}. The red lines are the β_{dyn} model isolines at 10 values of T_{ww} (Equation 16 of the main article). These isolines clearly follow the color gradient of the PHM results indicating that β_{dyn} is able to capture the complexity of a PHM.

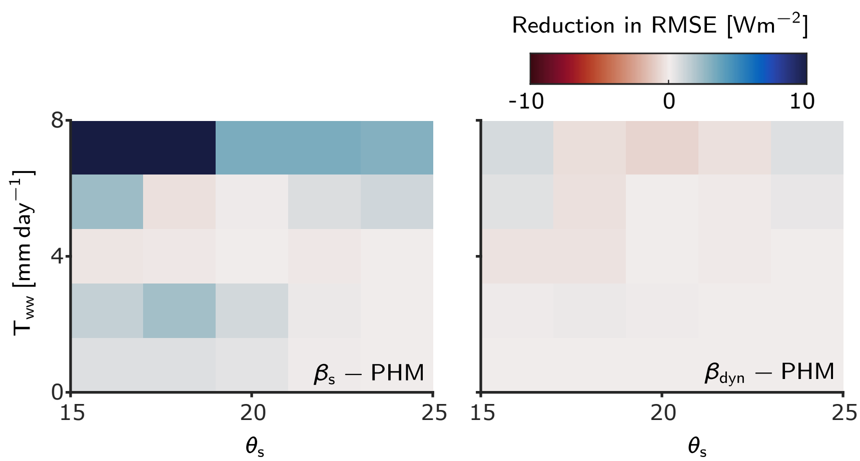

Figure S13. Analogous results to Fig. 5e-f in the main text using root mean square error instead of percent bias as the performance metric. The differences in reduction of RMSE between the PHM and β_s scheme (left) and β_{dyn} scheme (right).

Table S7. Cumulative total for evapotranspiration (ET), gross primary productivity (GPP), sensible heat flux (H), net radiative flux (R_n), and longwave radiative flux (L_{out}) for AmeriFlux US-Me2 data and 5 LSM simulations during high atmospheric moisture demand ($T_{ww} > 4\,mm\,day^{-1}$) for May-Aug 2013-2014. The surface energy fluxes are in units of cm H_2O and GPP is in units kg CO_2. The values in parentheses are the percent error compared to the observations.

	ET [cm]	**GPP [kg]**	**H [cm]**	**R_n [cm]**	**L_{out} [cm]**
Obs	26.5	2.9	48.4	94.2	69.5
WW	32.2 (21.4%)	3.6 (25.1%)	45.6 (-5.9%)	80.8 (-14.3%)	76.8 (10.5%)
PHM	26.7 (0.7%)	3 (4%)	50.1 (3.4%)	79.8 (-15.3%)	77.8 (11.9%)
β_s	28 (5.9%)	3.1 (9.1%)	49 (1.1%)	80 (-15.1%)	77.5 (11.6%)
β_{2L}	27.6 (4.2%)	3.1 (7.3%)	49.3 (1.8%)	80 (-15.2%)	77.6 (11.7%)
β_{dyn}	26.8 (1%)	3 (4.5%)	50 (3.2%)	79.8 (-15.3%)	77.8 (11.9%)

Table S8. Same as Table S7 except for during periods of low atmospheric moisture demand ($T_{ww} < 4\,mm\,day^{-1}$).

	ET [cm]	**GPP** [kg]	**H** [cm]	**R_n** [cm]	**L_{out}** [cm]
Obs	11.4	1.6	16.2	24.8	54.8
WW	9.7 (-15.3%)	2.4 (52.9%)	11.6 (-28.3%)	22 (-11.3%)	56.2 (2.5%)
PHM	9 (-21%)	2.3 (46.5%)	12.2 (-24.8%)	21.9 (-11.7%)	56.3 (2.7%)
β_s	8.8 (-22.7%)	2.3 (44.3%)	12.4 (-23.8%)	21.8 (-11.8%)	56.3 (2.8%)
β_{2L}	8.7 (-23.6%)	2.3 (43.2%)	12.5 (-23.3%)	21.8 (-11.9%)	56.3 (2.8%)
β_{dyn}	9 (-21.1%)	2.3 (46.4%)	12.2 (-24.8%)	21.9 (-11.7%)	56.3 (2.7%)

S7 Defining a Threshold for Transport-limitation

Quantifying the values of particular soil parameters and plant hydraulic traits that define a soil-plant system as transport-limited is an important avenue of future work. Fig. 3 in the article illustrates clearly that, even in the minimalist model, there is a complex interplay of drivers that contribute to the differences between PHM and β and, in turn, if a system is transport- or supply-limited. However, the overall soil-plant conductance in the minimalist model seems to be the main control on transport-limitation and a $g_{sp} \approx 30$ mm day^{-1}MPa^{-1} appears to be at the boundary between soil- and transport-limited conditions (Fig. S14). The definition of transport-limitation is somewhat subjective as it depends on how much difference between PHM and β is considered acceptable.

Determining a threshold of transport-limitation for the complex PHM is even less clear given the additional parameters. Therefore, a sensitivity analysis was performed using the recent Variogram Analysis of the Response Surface (VARS) method[45] implemented with the VARSTOOL package in MATLAB[39]. Our metric (M_{dif}, Eq. S109) to quantify the performance of each parameter set is the integrated difference in β and PHM-generated relative transpiration at high T_{ww} (5 mm day^{-1}) normalized by the difference between soil water content at incipient (θ_o) and complete (θ_c) stomatal closure. The normalization was an attempt to control for the differing ranges of soil moisture experienced by the plant; however, it had minimal impact on defining our transport-limitation threshold. The ranges and sensitivity scores for the 8 selected PHM parameters are shown in Table S9.

$$M_{dif} = \frac{1}{T_{ww} \cdot (\theta_o - \theta_c)} \cdot \int_{\psi_s} T^{\beta}(\psi_s) - T^{phm}(\psi_s, T_{ww})\, d\psi_s \tag{S109}$$

The VARSTOOL analysis reveals that the maximum xylem-to-leaf conductance ($g_{xl,max}$) is the most sensitive parameter; thus, as maximum conductance in the plant decreases, a single β curve becomes increasingly ineffective at downregulating transpiration realistically. The next most sensitive parameters are $\psi_{x,50}$, b, $\psi_{l,50}$, b_l, and a, but they are of secondary importance. Lastly, the remaining two soil parameters, $\psi_{s,sat}$ and $g_{sx,max}$, were found to be the least sensitive parameters because transport-limitation from soil is primarily controlled by b.

Focusing on $g_{xl,max}$, we estimate a threshold for transport-limitation similar to the minimalist model. We do so by parsing the $g_{xl,max}$ range into 14 bins and sampling 5000 parameter sets from each bin (the 7 other parameters are sampled from their entire range in Table S9 for this analysis). The resulting sensitivity metrics were plotted for each bin in Fig. S14. As $g_{xl,max}$ becomes lower ($g_{xl,max} < 30$ mm day^{-1}MPa^{-1}) there is a tendency for the PHM results to diverge substantially from those of a single β curve. This threshold notably coincides with that predicted by the minimalist model. The large amount of spread is likely caused by the interactions amongst the other parameters. Further work must be done to create a more robust relationship based on measurable plant and soil hydraulic parameters.

Table S9. VARSTOOL results for plant hydraulics model based on 35,600 parameter sets created using Progressive Latin Hypercube Sampling and 200 STAR sampling centers. The IVARS50 is an integrated metric of sensitivity that accounts for correlation of nearby parameter values in the parameter space. The sources for each parameter are how we determined a realistic range to sample from.

Parameter	Description	Range	Units	IVARs50	Sources
$g_{xl,max}$	Max xylem-to-leaf conductance	$[10^{-10},10^{-3}]$	$\frac{m}{sMPa}$	1.6e-3	[24,46]
$\psi_{x,50}$	Xylem water potential at 50% loss of conductance	[-0.1,-15]	MPa	8.0e-4	[29,47,48]
b	Soil retention curve exponent	[2,14]	-	1.5e-5	[26]
$\psi_{l,50}$	Leaf water potential at 50% stomatal closure	[-0.1,-15]	MPa	3.5e-4	[24]
a	Xylem vulnerability curve shape parameter	[0.2,10]	-	2.4e-4	[33]
b_l	Leaf vulnerability curve shape parameter	[0.2,5]	-	1.0e-4	[33]
$g_{sx,max}$	Max soil-to-xylem conductance	$[10^{-2},10^{3}]$	$\frac{m}{sMPa}$	3.0e-5	[24,35]
ψ_{sat}	Saturated soil water potential	$[10^{-3},10^{-2}]$	MPa	3.2e-6	[26]

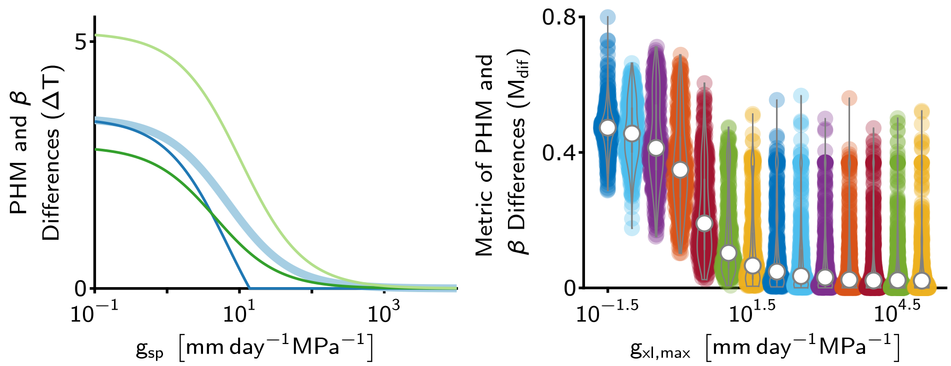

Figure S14. The control of soil-plant conductance (g_{sp}) on transport-limitation of a soil-plant system. Left: Differences in minimalist PHM and β as a function of overall soil-plant conductance. The thick light blue line represents change in g_{sp} with three other drivers at baseline values (see Fig. 3 in main article) while the thin lines represent 50% increase in ψ_s (dark blue), T_{ww} (light green) and $\psi_{l,c} - \psi_{l,o}$ (dark green) compared to their baseline values. Right: Differences between a more complex formulation of PHM and β used in the LSM analysis with respect to maximum xylem-to-leaf conductance. The metric used integrates the difference between relative transpiration of β and PHM at a $T_{ww} = 5\,mm\,day^{-1}$ normalized by the range of soil water availability over which downregulation occurs (Eq. S109).

References

1. Bonan, G. B. *et al.*: Modeling canopy-induced turbulence in the Earth system: a unified parameterization of turbulent exchange within plant canopies and the roughness sublayer (CLM-ml v0). *Geosci. Model. Dev* 11, 1467–1496, https://doi.org/10.5194/gmd-11-1467-2018, 2018.

2. Oleson, K. W. *et al.* Technical Description of the version 5.0 of the Community Land Model (CLM). Tech. Rep., National Center for Atmospheric Research, Boulder, 2018.

3. Goudriaan, J. & Laar, H. H. v.: Modelling potential crop growth processes : textbook with exercises (Springer Science and Business Media Dordrecht, Wageningen, 1994), first edn.

4. Sellers, P. J.: Canopy reflectance, photosynthesis and transpiration. *Int. J. Remote. Sens.* https://doi.org/10.1080/01431168508948283, 1985.

5. Bonan, G.: Climate Change and Terrestrial Ecosystem Modeling (Cambridge University Press, 2019).

6. Kowalczyk, E. A. *et al.* The land surface model component of ACCESS: description and impact on the simulated surface climatology. Tech. Rep., 2013.

7. De Pury, D. G. & Farquhar, G. D.: Simple scaling of photosynthesis from leaves to canopies without the errors of big-leaf models. *Plant, Cell Environ.* 20, 537–557, https://doi.org/10.1111/j.1365-3040.1997.00094.x, 1997.

8. Goudriaan, J.: Crop micrometeorology: a simulation study. Ph.D. thesis, Wageningen, 1977.

9. Dai, Y. *et al.*: A Two-Big-Leaf Model for Canopy Temperature, Photosynthesis, and Stomatal Conductance. *J. Clim.* 17, 2281–2299, https://doi.org/10.1175/1520-0442(2004)017<2281:ATMFCT>2.0.CO;2, 2004.

10. Brutsaert, W.: Evaporation into the Atmosphere: Theory, History and Applications (Kluwer Academic Publishers, 1982).

11. Monteith, J. & Unsworth, M.: Principles of Environmental Physics: Plants, Animals, and the Atmosphere: Fourth Edition (2013).

12. Oleson, K. W. *et al.* Technical Description of version 4.5 of the Community Land Model (CLM). Tech. Rep., National Center for Atmospheric Research, 2013. https://doi.org/10.5065/D6RR1W7M.

13. Medlyn, B. E. *et al.*: Reconciling the optimal and empirical approaches to modelling stomatal conductance. *Glob. Chang. Biol.* 17, 2134–2144, https://doi.org/10.1111/j.1365-2486.2010.02375.x, 2011.

14. Farquhar, G. D., von Caemmerer, S. & Berry, J. A.: A biochemical model of photosynthetic CO2 assimilation in leaves of C3 species. *Planta* 149, 78–90, https://doi.org/10.1007/BF00386231, 1980.

15. Damour, G., Simonneau, T., Cochard, H. & Urban, L.: An overview of models of stomatal conductance at the leaf level. *Plant, Cell Environ.* 33, 1419–1438, https://doi.org/10.1111/j.1365-3040.2010.02181.x, 2010.

16. Campbell, G. S. & Norman, J. M.: An Introduction to Environmental Biophysics-Second Edition- (1998).

17. Collatz, G., Ball, J., Grivet, C. & Berry, J. A.: Physiological and environmental regulation of stomatal conductance, photosynthesis and transpiration: a model that includes a laminar boundary layer. *Agric. For. Meteorol.* 54, 107–136, https://doi.org/10.1016/0168-1923(91)90002-8, 1991.

18. Bernacchi, C. J., Singsaas, E. L., Pimentel, C., Portis Jr, A. R. & Long, S. P.: Improved temperature response functions for models of Rubisco-limited photosynthesis. *Plant, Cell Environ.* 24, 253–259, https://doi.org/10.1111/j.1365-3040.2001.00668.x, 2001.

19. Leuning, R.: Temperature dependence of two parameters in a photosynthesis model. *Plant, Cell Environ.* 25, 1205–1210, https://doi.org/10.1046/j.1365-3040.2002.00898.x, 2002.

20. Bernachhi, C. J., C., P. & Long, S. P.: In vivo temperature response functions of parameters required to model RuBP-limited photosynthesis. *Plant, Cell Environ.* 26, 1419–1430, https://doi.org/10.1046/j.0016-8025.2003.01050.x, 2003.

21. Hirose, T. & Werger, M. J. A.: Maximizing daily canopy photosynthesis with respect to the leaf nitrogen allocation pattern in the canopy. *Oecologia* 72, 520–526, https://doi.org/10.1007/BF00378977, 1987.

22. Wang, Y.-P. & Leuning, R.: A two-leaf model for canopy conductance, photosynthesis and partitioning of available energy I: Model description and comparison with a multi-layered model. *Agric. For. Meteorol.* 91, 89–111, 1998.

23. Kennedy, D. *et al.*: Implementing Plant Hydraulics in the Community Land Model, Version 5. *J. Adv. Model. Earth Syst.* 11, 485–513, https://doi.org/10.1029/2018MS001500, 2019.

24. Manzoni, S., Vico, G., Katul, G., Palmroth, S. & Porporato, A.: Optimal plant water-use strategies under stochastic rainfall. *Water Resour. Res.* 50, 1–16, https://doi.org/10.1002/2014WR015375, 2014.

25. Feng, X. *et al.*: The ecohydrological context of drought and classification of plant responses. *Ecol. Lett.* 21, 1723–1736, https://doi.org/10.1111/ele.13139, 2018.

26. Clapp, R. B. & Hornberger, G. M.: Empirical equations for some soil hydraulic properties. *Water Resour. Res.* 14, 601–604, https://doi.org/10.1029/WR014i004p00601, 1978.

27. Daly, E. *et al.*: Coupled Dynamics of Photosynthesis, Transpiration, and Soil Water Balance. Part I: Upscaling from Hourly to Daily Level. *J. Hydrometeorol.* 5, 546–558, https://doi.org/10.1175/1525-7541(2004)005<0546:CDOPTA>2.0.CO;2, 2004.

28. Pammenter, N. W. & Willigen, C. V.: A mathematical and statistical analysis of the curves illustrating vulnerability of xylem to cavitation. *Tree Physiol.* 18, 589–593, https://doi.org/10.1093/treephys/18.8-9.589, 1998.

29. Klein, T.: The variability of stomatal sensitivity to leaf water potential across tree species indicates a continuum between isohydric and anisohydric behaviours. *Funct. Ecol.* 28, 1313–1320, https://doi.org/10.1111/1365-2435.12289, 2014.

30. Sperry, J. S., Adler, F. R., Campbell, G. S. & Comstock, J. P.: Limitation of plant water use by rhizosphere and xylem conductance: Results from a model. *Plant, Cell Environ.* 21, 347–359, https://doi.org/10.1046/j.1365-3040.1998.00287.x, 1998.

31. Pastorello, G. *et al.*: The {FLUXNET2015} dataset and the {ONEFlux} processing pipeline for eddy covariance data. *Sci. Data* 7, 225, https://doi.org/10.1038/s41597-020-0534-3, 2020.

32. Law, B. E.: AmeriFlux US-Me2 Metolius mature ponderosa pine. Ver. 16-5., https://doi.org/doi.org/10.17190/AMF/1246076, 2021.

33. Kattge, J. *et al.*: TRY plant trait database – enhanced coverage and open access. *Glob. Chang. Biol.* 26, 119–188, https://doi.org/10.1111/gcb.14904, 2020.

34. Schwarz, P. A. *et al.*: Climatic versus biotic constraints on carbon and water fluxes in seasonally drought-affected ponderosa pine ecosystems. *Glob. Biogeochem. Cycles* 18, 1–17, https://doi.org/10.1029/2004GB002234, 2004.

35. Jackson, R. B., Mooney, H. A. & Schulze, E. D.: A global budget for fine root biomass, surface area, and nutrient contents. *Proc. Natl. Acad. Sci. United States Am.* 94, 7362–7366, https://doi.org/10.1073/pnas.94.14.7362, 1997.

36. Maherali, H. & DeLucia, E. H.: Xylem conductivity and vulnerability to cavitation of ponderosa pine growing in contrasting climates. *Tree Physiol.* 20, 859–867, https://doi.org/10.1093/treephys/20.13.859, 2000.

37. Irvine, J. *et al.* Age-related changes in ecosystem structure and function and effects on water and carbon exchange in ponderosa pine. Tech. Rep. 7, 2004. https://doi.org/10.1093/TREEPHYS/24.7.753.

38. DeLucia, E. H. & Heckathorn, S. A.: The effect of soil drought on water-use efficiency in a contrasting Great Basin desert and Sierran montane species. *Plant, Cell & Environ.* 12, 935–940, https://doi.org/10.1111/j.1365-3040.1989.tb01973.x, 1989.

39. Razavi, S., Sheikholeslami, R., Gupta, H. V. & Haghnegahdar, A.: VARS-TOOL: A toolbox for comprehensive, efficient, and robust sensitivity and uncertainty analysis. *Environ. Model. Softw.* 112, 95–107, https://doi.org/10.1016/j.envsoft.2018.10.005, 2019.

40. Taylor, K. E.: Summarizing multiple aspects of model performance in a single diagram. *J. Geophys. Res. Atmospheres* 106, 7183–7192, https://doi.org/10.1029/2000JD900719, 2001.

41. Beven, K. & Binley, A.: GLUE: 20 years on. *Hydrol. Process.* 28, 5897–5918, https://doi.org/10.1002/hyp.10082, 2014.

42. FLUXNET: FLUXNET2015 Dataset, 2021.

43. Jackson, R. B. *et al.*: A global analysis of root distributions for terrestrial biomes, https://doi.org/10.1007/BF00333714, 1996.

44. Foken, T.: The energy balance closure problem: An overview. *Ecol. Appl.* 18, 1351–1367, https://doi.org/10.1890/06-0922.1, 2008.

45. Razavi, S. & Gupta, H. V.: A new framework for comprehensive, robust, and efficient global sensitivity analysis: 2. Application. *Water Resour. Res.* 52, 440–455, https://doi.org/10.1002/2015WR017559, 2016.

46. Couvreur, V. *et al.*: Water transport through tall trees: A vertically explicit, analytical model of xylem hydraulic conductance in stems. *Plant, Cell & Environ.* 41, 1821–1839, https://doi.org/10.1111/pce.13322, 2018.

47. Manzoni, S. *et al.*: Optimizing stomatal conductance for maximum carbon gain under water stress: a meta-analysis across plant functional types and climates. *Funct. Ecol.* 25, 456–467, https://doi.org/10.1111/j.1365-2435.2010.01822.x, 2011.

48. Choat, B. *et al.*: Global convergence in the vulnerability of forests to drought. *Nature* 491, 752–755, https://doi.org/10.1038/nature11688, 2012.